

Original Article

Cite this article: Zhao Z-x, Xu W-j, Dong G-c, Santosh M, Li H-b, and Chang Z-g (2023) Granitic magmatism associated with gold mineralization: evidence from the Baizhangzi gold deposit, in the northern North China Craton. *Geological Magazine* **160**: 1211–1227. <https://doi.org/10.1017/S0016756823000341>

Received: 4 August 2022

Revised: 11 May 2023

Accepted: 16 May 2023

First published online: 21 June 2023


Keywords:

adakitic rock; Baizhangzi; fractional crystallization; gold mineralization; late Triassic; Western Liaoning

Corresponding author: Guo-chen Dong;

Email: donggc@cugb.edu.cn

Granitic magmatism associated with gold mineralization: evidence from the Baizhangzi gold deposit, in the northern North China Craton

Zhi-xiong Zhao^{1,2} , Wei-jun Xu^{1,3}, Guo-chen Dong¹, M Santosh^{1,4}, Hong-bin Li¹ and Ze-guang Chang¹

¹School of Earth Science and Resources, China University of Geosciences, Beijing, China; ²Ulanqab Key Laboratory of Geospatial Big Data Application and Environmental Monitoring, Jining Normal University, Ulanqab, China; ³Rixing Mining Co. Limited of Lingyuan, Liaoning, China and ⁴Department of Earth Science, University of Adelaide, Adelaide, Australia

Abstract

The relationship between magmatism and gold mineralization has been a topic of interest in understanding the formation of ore deposits. The Baizhangzi gold deposit, located in the northern margin of the North China Craton, is hosted by the Baizhangzi granite (BZG) and provides a case to evaluate the relation between granite and gold mineralization in Late Triassic. In this study, we present petrography, bulk geochemistry, zircon U-Pb isotope and trace elements data, as well as major elements of biotite and plagioclase for the BZG to evaluate the petrogenesis and link with gold mineralization. The BZG comprises biotite monzogranite, biotite-bearing monzogranite and monzogranite (BZGs). Zircon U-Pb geochronology shows that all the granitoids of BZGs were coeval with a formation age of 232 Ma. The granitoids, with high SiO₂, Al₂O₃ and Sr, while low Y and Yb, show adakitic affinity. They are enriched in LILFs (e.g., Rb, Ba, Th, U and Sr) and LREEs, while depletion in HFSEs (e.g., Nb, Ta, P and Ti). The geochemical and mineral chemical data suggest that the granitoids have experienced the fractional crystallization of biotite + plagioclase + K-feldspar + apatite. Crystallization temperature is estimated as ca. 700°C, and pressure is between 0.71 kbar and 1.60 kbar. The monzogranite shows higher values of log f_{O_2} , Δ_{FMQ} and Δ_{NNO} than the biotite-bearing monzogranite, ranging from -19.76 to -11.71, -4.93 to +3.67 and -5.48 to +3.11, respectively. The fractional crystallization, together with high f_{O_2} , K-metasomatism and low evolution degree, provided favourable conditions for gold mineralization.

1. Introduction

The intrusion-related gold deposits (IRGDs) exhibit that the gold mineralization is spatially and temporally associated with the granitoids (Goldfarb *et al.* 2001; Lang & Baker, 2001). They mainly contain intrusion-hosted, proximal and distal deposit styles (Dressel *et al.* 2018). The characteristics of the latter two types are the relationship between the structural setting and their ore-forming process (Cepedal *et al.* 2013; Tuduri *et al.* 2018), for instance, the Fuwen Au-dominated Au-Ag deposit (Xu *et al.* 2017) and Numao gold deposit (Leal *et al.* 2022). However, the intrusion-hosted deposits are characterized by the direct effect of magmatism on gold mineralization (Lang & Baker, 2001), such as the Linares deposit (Cepedal *et al.* 2013), Bilihe gold deposit (Yang *et al.* 2016) and the Julia deposit (Soloviev *et al.* 2022). The IRGDs have been intensively studied, and the role of magmatism in gold mineralization is a subject of debate. However, there is a consensus on the basically consistent time of magmatism and mineralization (e.g. Yang *et al.* 2016; Wang *et al.* 2020; Liu *et al.* 2021; Soloviev *et al.* 2022). In summary, four different aspects have been stressed: (1) the origin of magma, such as reworking of an ancient crust is related to the formation of gold in the Argun massif (Liu *et al.* 2022); (2) fractional crystallization, for instance, highly fractionated quartz diorite porphyry is related to the Bilihe gold deposit (Yang *et al.* 2016); (3) composition (type, volatiles, K₂O content and alkalinity), for example adakitic granitoids have genetic links to the Fuwen Au-Ag ore deposit (e.g. Zorin *et al.* 2001; Xu *et al.* 2017); ilmenite-series igneous rocks are related to the Bilihe gold deposit (Yang *et al.* 2016); higher volatiles, K and alkaline are more conducive to the gold mineralization in the northern margin of the North China Craton and Xiaoqinling (e.g. N'dri *et al.* 2021; Liu *et al.* 2022); and (4) high oxygen fugacity. Furthermore, Blevin (2004) has assessed the relationships of magmatic-hydrothermal mineralization associated with an igneous suite, suggesting that (1) silica distributions 'skewed' to high values are typically associated with Au, (2) K/Rb ratios greater than 200 are associated with Cu-Au systems, (3) the degree and type of fractionation

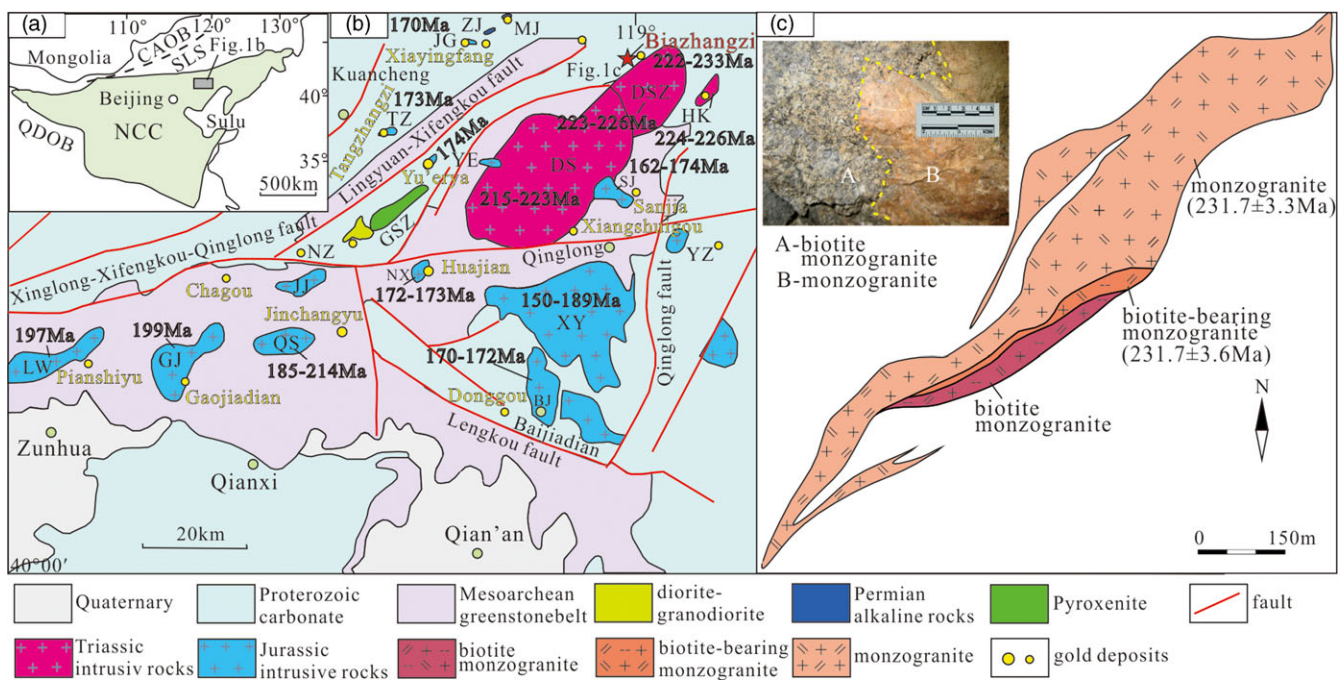


Figure 1. (Colour online) (a) Tectonic map of the North China Craton (Jiang *et al.* 2013), CAOB – Central Asian Orogenic Belt, SLS – Solonker suture, QDOB – Qinling-Dabie Orogenic Belt. (b) Sketch geological map of the LX district showing the distribution of gold deposits and igneous rocks with ages (modified from Xiong *et al.* 2017; Zhang *et al.* 2020). (c) Sketch map of BZG at the 30m level with photos of contact relationship. Intrusive rocks: BJ – Baijiadian, DS – Dushan, DSZ – Dashizhuizi, GJ – Gaojiadian, GSZ – Gushanzi, HK – Hekanzi, JG – Jinbaogou, JJ – Jiashan, LW – Luowenyu, MJ – Maojiagou, NX – Niuxinshan, QS – Qingshankou, SJ – Sanjia, TZ – Tangzhangzi, YZ – Yangzhangzi, ZJ – Zhaojiashuang.

determine the potential for mineralization and the type of mineralization and (4) the relative oxidation state control the compatible or incompatible nature of the ore. These investigations suggest that the composition, magmatic process and physiochemical conditions are effective parameters to assess the relationship between magmatism and gold mineralization.

The North China Craton (NCC) is one of the major gold-producing regions in China, and over 60% of the gold deposits are hosted by or are related to Phanerozoic intrusions (Nie *et al.* 2004; Deng & Wang, 2016; Yang & Santosh, 2020). These gold deposits have been classified as either IRGDs (Sillitoe & Thompson, 1998) or orogenic gold deposits (Goldfarb *et al.* 2001; Miao *et al.* 2005; Goldfarb & Groves, 2011; Groves & Santosh, 2016; Santosh & Groves, 2022). It is, therefore, of great significance to study the relationship between magmatism and gold mineralization.

There are many gold deposits defining gold ore concentration in the eastern Hebei – western Liaoning area in the northern margin of the NCC (Kong *et al.* 2015). These deposits are mostly medium to large scale in the ore reserves and are distributed as ‘satellites’ around the Dushan batholith (DSB) (Fig. 1b), such as Yu’erya, Jinchangyu, Huajian, Baizhangzi, etc. They are closely related to the Mesozoic alkaline to calc-alkaline intrusive rocks, directly hosted by, or located in the vicinity of igneous rocks with almost the same mineralization age as that of magmatism (Chen *et al.* 2019; Zhang *et al.* 2020), indicating a typical IRGD characteristic according to Lang and Baker (2001) and Goldfarb *et al.* (2001). These gold deposits have long been studied (e.g. Sillitoe & Thompson, 1998; Miao *et al.* 2008; Chen *et al.* 2014; Song *et al.* 2016; Bai *et al.* 2019), with the understanding that the gold mineralization is related to the magmatism. For example, the Jinchangyu gold deposit was regarded as IRGD type by Sillitoe and Thompson (1998) and further considered to be related to the DSB

(Luo *et al.* 2001), while the Yu’erya gold deposit together with its hosted intrusion is identified as the product of partial melting in the lower crust during early Yanshan Movement (Chen *et al.* 2014), and the Baizhangzi gold deposit is thought to be related to the Late Triassic magmatism (Miao *et al.* 2008).

The Baizhangzi gold deposit, one of the typical IRGDs, is hosted by the Baizhangzi granite (BZG). Previous studies reported zircon SHRIMP (222 ± 3 Ma) (Luo *et al.* 2004) and LA-ICP-MS age (233 ± 3 Ma) (Xiong *et al.* 2017) of the BZG. The ore formation mechanism and metallogenic prognosis (Wang, 1989; Wei *et al.* 2016; Wang *et al.* 2018) were also reported. However, the factors which are conducive to the gold mineralization during the magmatic process have not been clarified. In this study, we present detailed petrography, bulk geochemistry, zircon U-Pb isotope and trace element data, as well as EPMA mineral compositions, with a view to evaluate the magmatism associated with gold mineralization to provide guidelines for the future mineral exploration in the area.

2. Geological setting and petrology

2.a. Geological setting

The NCC, as one of the oldest cratons in the world with a basement rocks as old as 3.8 Ga (e.g. Zhai & Santosh, 2011), is bordered by the Central Asian Orogenic Belt (CAOB) in the north, the Qinling-Dabie Orogenic Belt (QDOB) in the south and the Sulu Orogen in the east (Fig. 1a). The basement of the NCC is composed of metamorphosed Archaean and Paleoproterozoic rocks, including tonalite-trondhjemite-granodiorite (TTG) gneisses, amphibolite and a few supracrustal rocks (Lu *et al.* 2008; Kong *et al.* 2015). These are overlain by post-Mesoproterozoic and Cambrian-

Ordovician marine clastic and carbonate rocks, Middle and Late Carboniferous marine and continental facies, Permian to Triassic fluvial and delta facies sedimentary rocks and Jurassic-Cretaceous sedimentary and volcanic rocks. After the final cratonization of the NCC during the late Paleoproterozoic at about 1.85 Ga (Wilde *et al.* 2002; Zhao & Zhai, 2013), the craton remained mostly stable prior to Triassic. During Mesozoic, the NCC witnessed intense magmatic activity during six stages: Early Triassic, Middle-Late Triassic, Early Jurassic-earliest Middle Jurassic, Middle-Late Jurassic, Early Cretaceous and Late Cretaceous (Zhang *et al.* 2014). Among them, Permian-Triassic magmatic rocks are widely distributed in the Yinshan and Yanshan belts along the northern margin of the NCC (Zhang *et al.* 2010). Middle-Late Triassic intrusive rocks are mainly distributed in the northern and eastern NCC, Liaodong and Korean Peninsula (Wu *et al.* 2005a, 2007). Early Jurassic-earliest Middle Jurassic igneous rocks are mainly distributed in the southern Yanbian area (Wu *et al.* 2011) and Western Hills of Beijing in the northern NCC (Liu *et al.* 2012). Middle-Late Jurassic magmatic rocks are widely distributed in the Yanshan Belt in the northern NCC, the Liaodong area and Jiaodong Peninsula in the eastern NCC, the southern Yanbian-Liaobei area in the northeastern NCC and in the northern part of North Korea (Wu *et al.* 2011). Early Cretaceous igneous rocks are widely distributed throughout the eastern and central NCC and are considered to be a 'giant igneous event' in eastern China (Wu *et al.* 2005b). Late Cretaceous magmatic rocks are relatively minor and distributed in the eastern part of the NCC (Zhang *et al.* 2011).

The eastern Hebei – western Liaoning district, located in the northern margin of the NCC, is underlain by gneiss, amphibolite and granulites of the Mesoarchean Badaohe Group (Fig. 1b), with Proterozoic carbonate and Quaternary cover (Miao *et al.* 2008; Zhang *et al.* 2020). Dozens of intrusive rocks occur in this area, including the Dushan, Dashizhu, Hekanzi, Xiaoyingzi, Qingshan and BZGs, etc. (Fig. 1b), which belong to three periods of magmatism (Miao *et al.* 2008): ~220 Ma, 190 Ma–200 Ma and ~170 Ma. Among them, the DSB is the largest with nearly 30 km in NE-SW and ~17 km in E-W and an elliptical shape area of over 450 km² (Miao *et al.* 2008). Previous zircon U-Pb dating reported ages of 215.3 Ma (Rao *et al.* 2002), 223 Ma (Luo *et al.* 2003), 221–222 Ma (Ye *et al.* 2014), 218 Ma (Jiang *et al.* 2018), 162 Ma and 170 Ma (Jiang *et al.* 2018), indicating magmatism during Late Triassic and Middle-Late Jurassic. There are a series of E-, NE- and NNE-trending faults and folds (Fig. 1b, e.g. EW-trending Xinglong-Xifengkou-Qinglong fault, Lingyuan fault extending NE-SW and Malanyu anticline) in the western Liaoning region (Zhang *et al.* 2020). The E-trending faults are generally parallel to the northern margin of the NCC, which is believed to be related to the southward subduction of the Paleo-Asian Ocean (Davis *et al.* 2001). The NE- to NNE-trending faults are in general parallel to the Tanlu fault, considered to be related to the subduction of the Pacific plate (Cox *et al.* 1989; Miao *et al.* 2008).

2.b. The Baizhangzi granitoid

The BZG, located 3 km north of the Dashizhu (DSZ) granite (Fig. 1b), is the main ore-bearing rock of the Baizhangzi gold deposit. It occurs as a stock or dike along the NNE-trending fault, with an exposed area of 1 km², intruding the Proterozoic clastic rocks and Triassic diorite (Luo *et al.* 2004; Xiong *et al.* 2017). Our field investigation and microscopic observation revealed that the Baizhangzi stock intrusion is composed of medium to fine biotite monzogranite, biotite-bearing monzogranite and monzogranite

(BZGs) (Fig. 1c). These granites are separated by transitional boundaries (Fig. 1c).

Biotite monzogranite occurs as medium to fine-grained, dark red rocks (Fig. 2a), composed of plagioclase (35–40%), K-feldspar (30–35%), quartz (ca. 20%) and biotite (10–15%) (Fig. 2b). Zircon, apatite and magnetite are accessory minerals. Plagioclase is often euhedral with prismatic to lath-like form, and a few crystals are selectively sericitized (Fig. 2c). K-feldspar is present as sub-euhedral to anhedral. Quartz commonly is anhedral. Biotite occurs as euhedral to sub-euhedral with strong pleochroism from yellowish brown to dark reddish brown, and a few of them are altered into chlorite.

Biotite-bearing monzogranite contains much less plagioclase (30–35%) and biotite (5–10%), while little more quartz (20–25%) (Fig. 2d). The accessory mineral types and alteration characteristics are the same as those of biotite monzogranite.

Monzogranite is constituted mainly by plagioclase (30–35%), K-feldspar (35–40%) and quartz (25%±), with <5% biotite (Fig. 2e, f). The accessory minerals are zircon, apatite and magnetite. These rocks occur as white or red colours, which is interpreted as silicification (Fig. 2g), and potassium alteration (Fig. 2h).

3. Analytical methods

3.a. LA-ICP-MS Zircon trace elemental and U-Pb dating

Zircon separations were performed at the Xinhang Institute of Surveying and Mapping in Hebei Province through panning, heavy liquid and magnetic separation. Around 180 zircons, with complete crystal shape, with no cracks and no inclusions, were selected under binocular and mounted with epoxy resin on a glass plate and polished. The transparent, reflected light and cathodoluminescence (CL) images were obtained at the Beijing Zhongke Mineral Research Testing Technology Co., Ltd. Zircon trace element and U-Pb analyses were conducted in the Beijing Zirconian Pilot Technology Co., Ltd., Beijing, China, using the UP 213 nm laser ablation system and Agilent 7500A ICP-MS produced by New Wave. Helium gas was used as carrier gas, and the laser beam diameter was 30 µm. One 91500 standard sample was used for calibration of test data at every 10 sample points. Andersen (2002) was used for the calibration of ordinary lead. ICPMSDataCal program (Liu *et al.* 2010) was used to process the data, and U-Pb age concordance plots were plotted using Isoplot 3.0 (Ludwig, 2003).

3.b. Whole-rock major and trace elements

The least altered samples were selected and crushed to less than 200 mesh. The whole-rock major and trace element compositions were analysed at the Wuhan SampleSolution Analytical Technology Co., Ltd., Wuhan, China. Major element oxides were measured by X-ray fluorescence spectrometer (XRF). Trace elements were determined using an Agilent 7700a ICP-MS. The standards for major and trace elements are GBW07103, GBW07105, GBW07111, and BHVO-2, BCR-2, RGM-2, respectively, and the relative standard deviation is <5% for both of them.

3.c. Electron probe microanalyses

The mineral compositions of the studied rocks were analysed using an electron microprobe analyser (EPMA; JXA-8100, JEOL) with a 15 kV accelerating voltage, 20 nA probe current and 5 µm beam diameter, at the Institute of Geology, Chinese Academy of

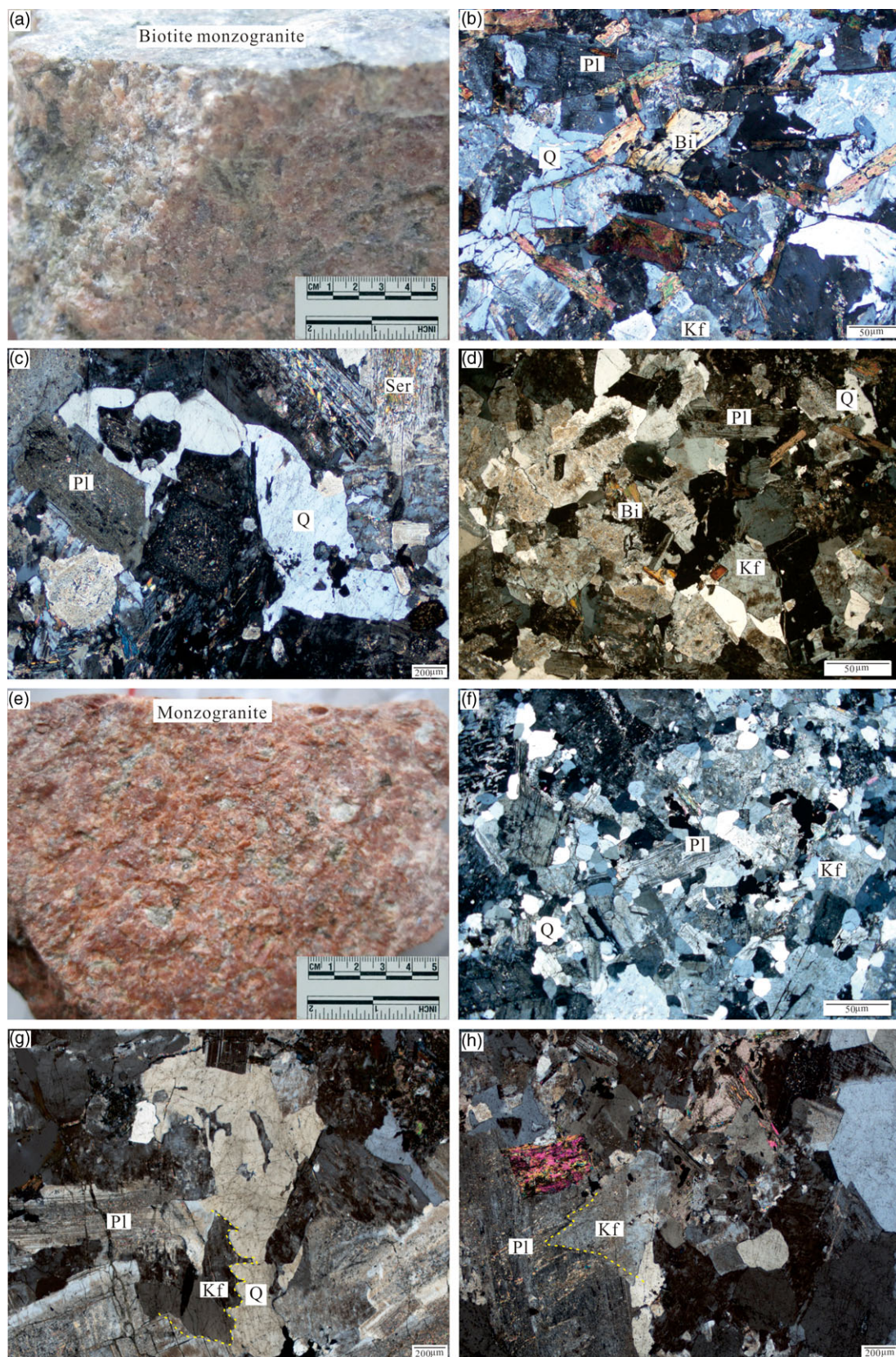


Figure 2. (Colour online) Photographs of BZGs. (a) and (b) Biotite Monzogranite. (c) Sericitization. (d) Biotite-bearing monzogranite. (e) and (f) Monzogranite. (g) Silicification (quartz metasomatic K-feldspar). (h) Potassium (K-feldspar) metasomatic plagioclase. **Ser** – sericite; **Bi** – biotite; **Kf** – K-feldspar; **Pl** – plagioclase; **Q** – quartz.

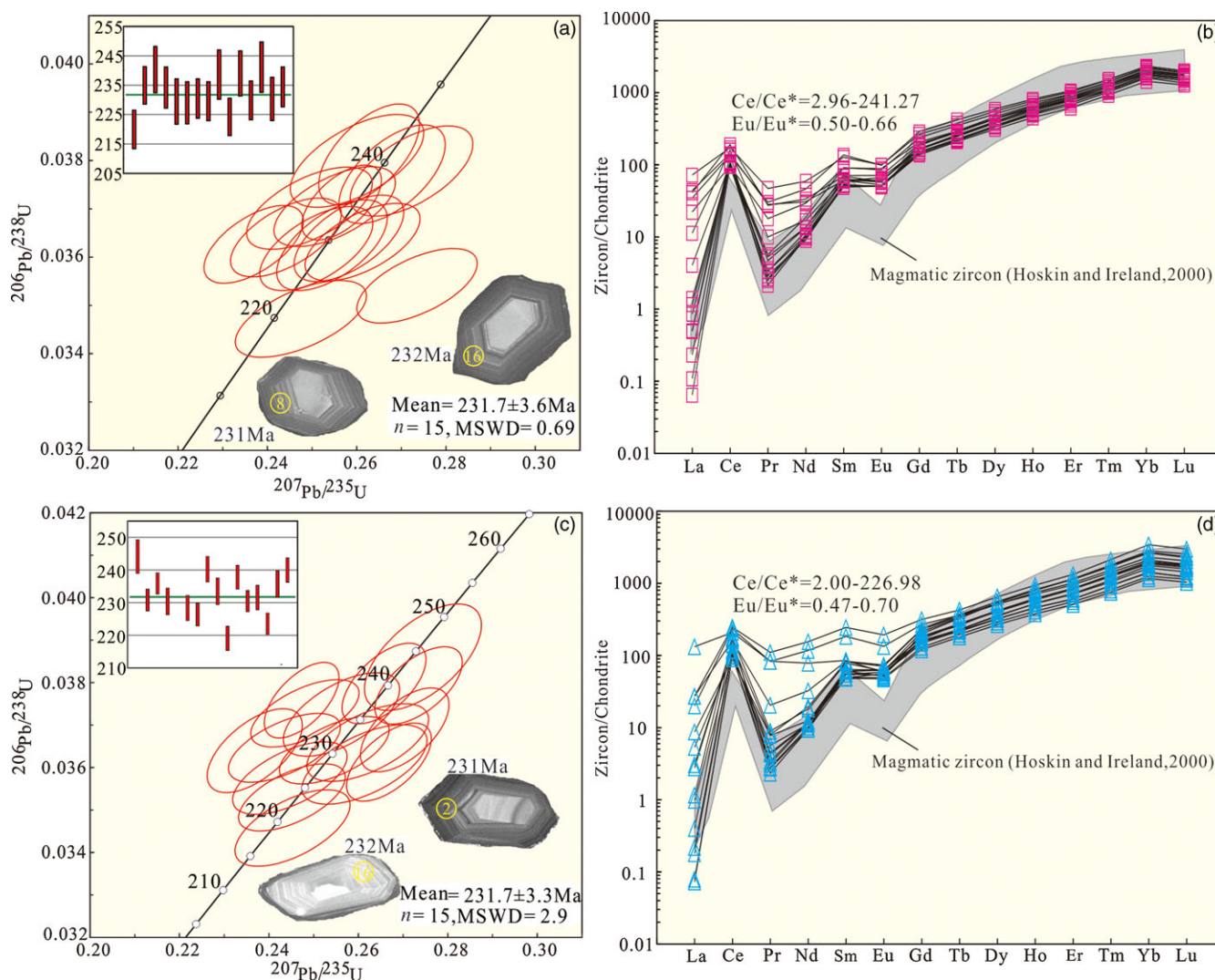


Figure 3. (Colour online) U–Pb concordia diagrams with cathodoluminescence (CL) images of representative zircons analysed and zircon chondrite-normalized REE patterns from the BZGs. (a) and (b) Biotite-bearing monzogranite (sample No. 0–8). (c) and (d) Monzogranite (sample No. -30–7). Chondrite values are from Sun and McDonough (1989).

Geological Science. SiO_2 , Al_2O_3 , MgO , MnO , CaO , Na_2O , K_2O , FeO , TiO_2 , Cr_2O_3 and NiO were analysed. Line and spectrometer crystal used for major element are as follows: Si ($\text{K}\alpha$, TAP), Na ($\text{K}\alpha$, TAP), K ($\text{K}\alpha$, PETJ), Al ($\text{K}\alpha$, TAP), Mg ($\text{K}\alpha$, TAP), Mn ($\text{K}\alpha$, LIFH), Fe ($\text{K}\alpha$, LIFH), Cr ($\text{K}\alpha$, LIFH), Ni ($\text{K}\alpha$, LIFH), Ti ($\text{K}\alpha$, PETJ) and Ca ($\text{K}\alpha$, PETJ). Count times were 10s for peak and 5s for background per element. Natural and synthetic minerals used for standardization are as follows: (1) for plagioclase: albite (Na and Al), K-feldspar (K), rutile (Ti), NiO (Ni), Cr_2O_3 (Cr), Fe_2O_3 (Fe), spessartite (Mn), diopside (Ca and Mg), plagioclase/K-feldspar (Si); (2) for biotite: albite (Na and Al), K-feldspar (K), rutile (Ti), NiO (Ni), Cr_2O_3 (Cr), Fe_2O_3 (Fe), spessartite (Mn), diopside (Ca), Biotite (Si and Mg). ZAF corrections were carried out. The estimated precisions for major elements are $\pm 2\%$.

4. Results

4.a. Zircon trace elemental and U–Pb ages

One sample each from the biotite-bearing monzogranite (No. 0–8) and monzogranite (No. -30–7) were selected for LA-ICP-MS zircon

U–Pb dating and trace elements. The analytical data are listed in Supplementary Tables S1, S2.

The zircon grains from both the biotite-bearing monzogranite and monzogranite are colourless and euhedral to subhedral. They show oscillatory zoning, without inherited cores in the CL images (Fig. 3a, c). The abundances of thorium and uranium of analysed spots range from 280 ppm to 1648 ppm, 245 ppm to 1390 ppm, respectively, corresponding to Th/U ratios between 0.92 and 1.35 (>0.4). Zircon shares light rare earth element (LREE)-inclined patterns, with varying contents of LREE, characteristics of the Ce-positive anomalies (Ce/Ce^*) and Eu-negative anomalies (Eu/Eu^*) (Fig. 3b, d), which are consistent with the characteristics of magmatic zircons (Hoskin & Ireland, 2000). All of such indicate a magmatic origin (Christopher *et al.* 2003; Jan & Sylvester, 2003; Randall & Stephen, 2003).

Fifteen zircons from sample 0–8 yielded $^{206}\text{Pb}/^{238}\text{U}$ ages from 230 to 238 Ma, with a weighted mean age of 231.7 ± 3.6 Ma (MSWD = 0.69) (Fig. 3a). Fifteen zircons in sample -30–7 yielded $^{206}\text{Pb}/^{238}\text{U}$ ages from 229 to 241 Ma, with a weighted mean age of 231.7 ± 3.3 Ma (MSWD = 2.9) (Fig. 3c). The two ages are almost identical to each other.

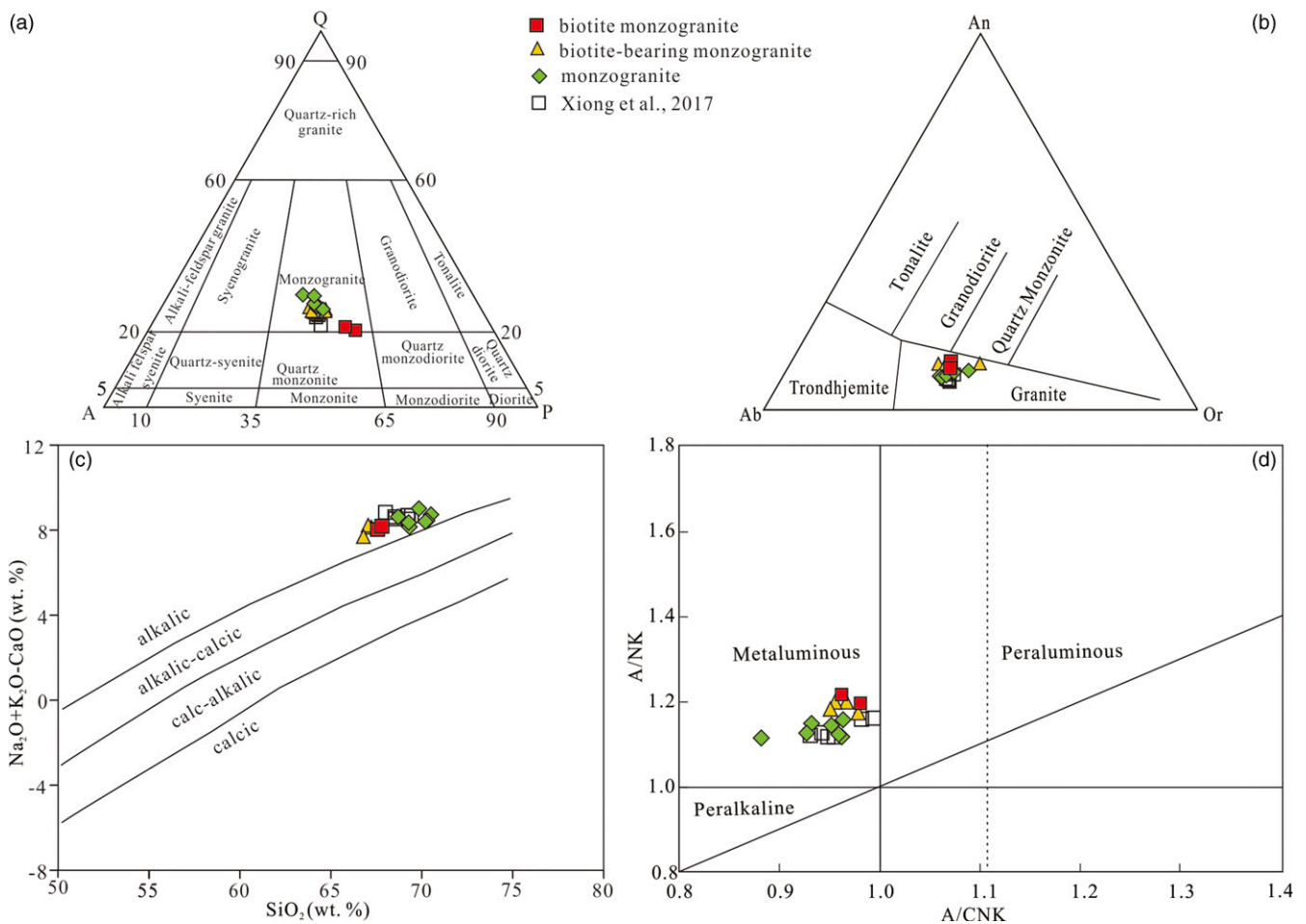


Figure 4. (Colour online) Classification diagrams of samples from the BZGs. (a) QAP diagram (Le Maitre, 2002). (b) An-Ab-Or diagram (Barker & Millard, 1979). (c) $(\text{Na}_2\text{O} + \text{K}_2\text{O} - \text{CaO})$ vs. SiO_2 (Frost *et al.* 2001). (d) A/NK vs. A/CNK diagram (Manillar & Piccoli, 1989).

4.b. Whole-rock major and trace element compositions

Two biotite monzogranites, four biotite-bearing monzogranites and seven monzogranites of the BZGs were analysed in this work. Whole-rock major and trace element compositions of these samples are listed in Supplementary Table S3. The following data of major elements are recalculated after removing the LOI.

The SiO_2 content of biotite monzogranite samples ranges from 67.57 to 67.81 wt%, and $\text{Na}_2\text{O} + \text{K}_2\text{O}$ ranges from 9.77 to 9.99 wt%. The data fall in the monzogranite field in the QAP diagram (Fig. 4a) and plot to the granite field in the An-Ab-Or diagram (Fig. 4b). The values of $\text{Na}_2\text{O} + \text{K}_2\text{O} - \text{CaO}$ range from 8.03 to 8.18 wt%, and the two data plot along with the alkaline series in a $(\text{Na}_2\text{O} + \text{K}_2\text{O} - \text{CaO})$ versus SiO_2 diagram (Fig. 4c). The Al_2O_3 content is between 15.75 and 16.38 wt%, with A/CNK values ranging from 0.96 to 0.98, and A/NK values between 1.20 and 1.22, identifying with the metaluminous field in an A/CNK versus A/NK diagram (Fig. 4d). The content of MgO ranges from 0.87 to 1.18 wt%, with the Mg values $(\text{nMg}^{2+} / (\text{nMg}^{2+} + \text{nFe}^{2+}) * 100)$ from 40.48 to 42.36. The biotite monzogranite shows similar chondrite-normalized rare earth element (REE) patterns (Fig. 5a), with being enriched in LREE ($\text{La}_N = 356.03\text{--}357.66$, $\text{Yb}_N = 6.21\text{--}6.53$ and $\text{La}_N/\text{Yb}_N = 54.8\text{--}57.4$) and insignificant Eu anomaly ($\text{Eu}/\text{Eu}^* = \text{Eu}_N / [(\text{Sm}_N) \times (\text{Gd}_N)]^{1/2} = 0.94\text{--}1.01$). A primitive-mantle-normalized trace element diagram (Fig. 5b) shows negative

anomalies for high field strength elements (HFSEs) (such as Nb, Ta, P and Ti) and variable enrichment in large ion lithophilic elements (LILEs) (for instance, Rb, Ba, Th, U and Sr), with high Sr (793–855 ppm).

The monzogranite exhibits higher SiO_2 (from 68.70 to 70.51 wt%), and $\text{Na}_2\text{O} + \text{K}_2\text{O}$ (9.87–10.25 wt%). In a QAP diagram (Fig. 4a), they all fall into the monzogranite field, which is consistent with plotted in the granite field in the An-Ab-Or diagram (Fig. 4b). The $\text{Na}_2\text{O} + \text{K}_2\text{O} - \text{CaO}$ contents vary widely, from 8.15 to 9.02, and the data mainly plot along with the alkalic series in a $(\text{Na}_2\text{O} + \text{K}_2\text{O} - \text{CaO})$ versus SiO_2 diagram (Fig. 4c). The Al_2O_3 content ranges from 15.16 to 15.56, with A/CNK and A/NK values 0.88–0.96, 1.11–1.16, respectively, corresponding to the metaluminous field in an A/CNK versus A/NK diagram (Fig. 4d). The MgO content ranges from 0.46 to 0.82 wt% (average of 0.66 wt%), with the Mg values $(\text{nMg}^{2+} / (\text{nMg}^{2+} + \text{nFe}^{2+}) * 100)$ from 29.23 to 47.31. The monzogranite shows similar characteristics in the chondrite-normalized REE diagram (Fig. 5c) and primitive-mantle-normalized trace element diagram (Fig. 5d) with the biotite monzogranite, while the lower Sr (420–612 ppm) and Eu/Eu^* (0.77–0.89) relatively, suggesting that the crystallization of plagioclase may have occurred.

The biotite-bearing monzogranite displays a coherent behaviour of major and trace elements with the other rock types

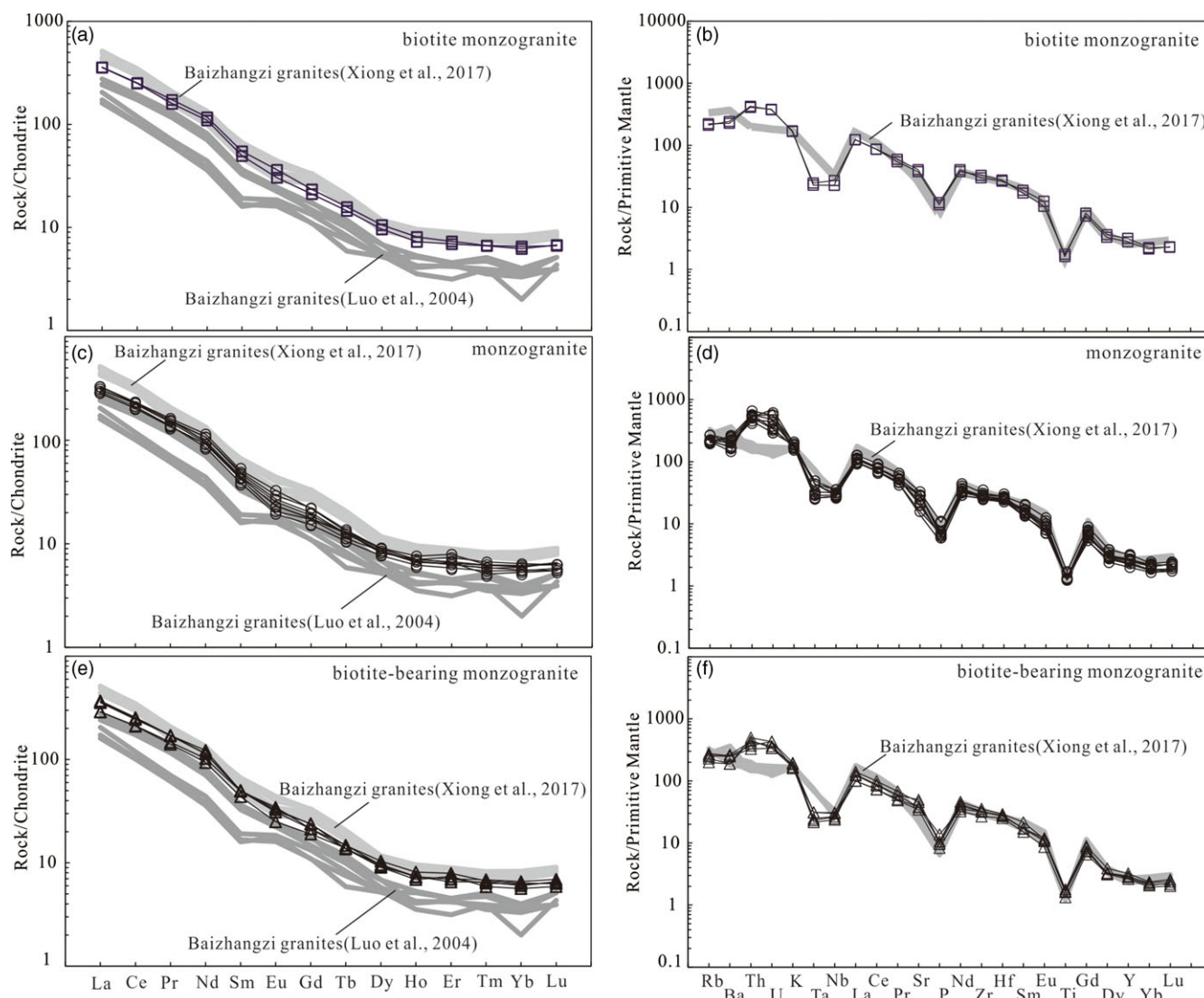


Figure 5. (Colour online) Chondrite-normalized rare earth element (REE) patterns (a, c, and e) and primitive-mantle-normalized trace element spider diagrams (b, d, and f) are shown. Chondrite values and primitive-mantle values are from Sun and McDonough (1989).

(Figs. 4, 5) suggesting that the biotite monzogranite, biotite-bearing monzogranite and monzogranite are likely cogenetic, and magma evolution may have played an important role in their formation.

For the BZGs, we used the samples of Xiong *et al.* (2017) and Luo *et al.* (2004).

4.c. Mineral geochemistry

Representative grains of plagioclase and biotite were analysed by microprobe for mineral chemistry.

4.c.1. Plagioclase

The following samples were analysed: thirteen plagioclases from the three biotite monzogranite samples (20BZ125, 20BZ126, 20BZ07), fourteen plagioclases from the three biotite-bearing monzogranite samples (120-1, 19BZ38, 20BZ16) and thirty-five plagioclases from the nine monzogranite samples (150-1, 0-12, 20BZ31, 20BAZ36, 108-12, -30-5, 20BZ01, 19BZ41, 19BZ35).

Plagioclase in the BZGs is generally fresh to slightly altered and euhedral to subhedral tabular crystals, exhibiting obvious polysynthetic twinning under cross-polarized light. In this study, unaltered regions of plagioclase were selected for chemical composition analysis; therefore, the analysis results are little or not affected by alteration. Some representative data are listed in Supplementary Table S4.

The major element contents of plagioclase from the biotite monzogranite are as follows: SiO₂ (63.5–67.9 wt%, average 65.7%), Al₂O₃ (19.5–23.0 wt%, average 20.8%), CaO (0.42–3.07 wt%, average 1.67%), FeO (0.08–0.58 wt%, average 0.23%), Na₂O (9.2–11.8 wt%, average 10.6%) and K₂O (0.1–0.8 wt%, average 0.36%), while An values range from An_{2.01} to An_{14.06}, with an average of An_{7.84}, corresponding to four of them belong to oligoclase and the other nine belong to albite in Ab–An–Or diagram (Fig. 6).

The plagioclase from the monzogranite has higher SiO₂ (ranges from 64.9 to 68.9 wt%, average 67.3%), Na₂O (9.3–12.3 wt%, average 11.3%) and K₂O (0.06–3.12 wt%, average 0.41%); however, lower Al₂O₃ (19.0–21.5 wt%, average 19.9%), CaO (0.006–1.7 wt%,

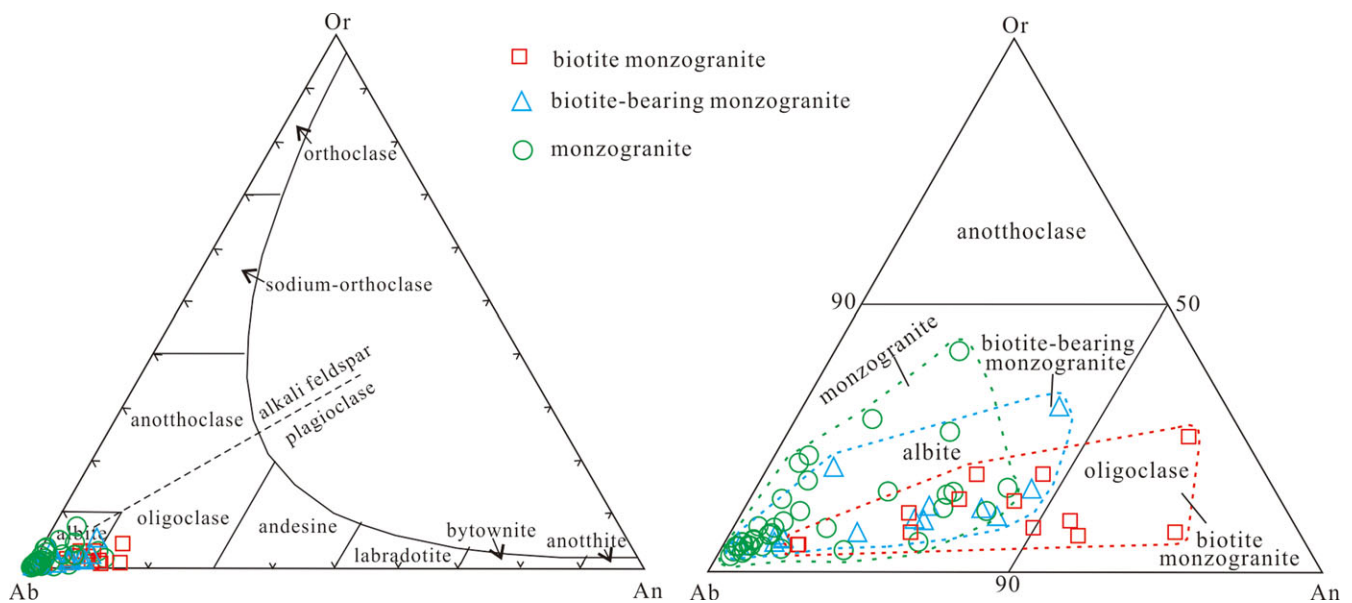


Figure 6. (Colour online) Ternary plots of plagioclase compositions (after Smith, 1974), and the right is a 5x magnification of the projection area of the left.

average 0.4%), FeO (0.003–0.66 wt%, average 0.17%) and An values (ranged from $An_{0.03}$ to $An_{7.78}$, with an average of $An_{2.02}$), corresponding to all of them belong to albite (Fig. 6).

The average major element contents of plagioclase from the biotite-bearing monzogranite are as follows: SiO_2 (66.8%), Al_2O_3 (20.2%), CaO (0.9%), Na_2O (10.9) and $An_{4.22}$, and all belong to albite (Fig. 6).

The composition and chemical formula of plagioclase listed in Supplementary Table S5 show that the number of Na, Ca, Al, Si from the biotite monzogranite ranges from 0.7922 to 1.0030 (average 0.9095), from 0.0198 to 0.1466 (average 0.0791), from 1.0098 to 1.2033 (average 1.0857), from 2.8205 to 2.9817 (average 2.9087), respectively. There are more Na and Si (average 0.9667, 2.9650, respectively), while less Ca and Al (average 0.0207, 1.0323, respectively) of the monzogranite. The number of cations (Na, Ca, Al, Si) lie between biotite monzogranite and monzogranite (average 0.9370, 0.0420, 1.0534, 2.9467, respectively) from the biotite-bearing monzogranite. The mean chemical formula of plagioclase from three types of rock are $(Na_{0.9095}, Ca_{0.0791}) [Al_{1.0857}Si_{2.9087}O_8]$, $(Na_{0.9370}, Ca_{0.0420}) [Al_{1.0534}Si_{2.9467}O_8]$ and $(Na_{0.9667}, Ca_{0.0207}) [Al_{1.0323}Si_{2.9650}O_8]$, respectively.

On the An vs. SiO_2 , Al_2O_3 , CaO, Na_2O , Ab, Or diagram (Fig. 7), plagioclase from the biotite-bearing monzogranite mostly plot between biotite monzogranite and monzogranite, exhibiting the same characteristic as the major and trace elements of the BZGs, which also suggests that the BZGs are products from co-genetic magma.

4.c.2. Biotite

The EPMA data and chemical formula of biotite are presented in Supplementary Table S6. The number of cations and related parameters is calculated using the Li (Li *et al.* 2020) method, based on the general formula of $A_1M_3T_4O_{10}W_2$.

The biotite from the biotite monzogranite shows SiO_2 from 34.61 wt% to 36.32wt% (average 35.67%), Al_2O_3 in the range of 13.54–14.59 wt% (average 13.86 wt%), FeO of 18.73–23.88 wt% (average 20.97 wt%), MgO of 9.80–12.15 wt% (average 11.55 wt%),

TiO_2 of 3.60–4.23 wt% (average 3.92 wt%) and K_2O of 7.98–8.96 wt% (average 8.58 wt%).

The biotite from the biotite-bearing monzogranite shows SiO_2 (35.27wt%), Al_2O_3 (13.29 wt%), FeO (21.23 wt%), MgO (12.92 wt%), TiO_2 (4.56 wt%) and K_2O (7.59 wt%).

The biotite from the monzogranite has the highest SiO_2 (36.92wt%) and MgO (13.16 wt%), while the lowest FeO (18.24 wt%) and TiO_2 (4.56 wt%).

Fe/(Fe+Mg) ratio ranges from 0.44 to 0.58, suggesting that they were not been altered by fluids (Stone, 2000), consistent with falling in the primary biotite field in the $10 \times TiO_2$ -FeO-MgO diagram (Fig. 8a). The Mg/(Fe+Mg) ratio is relatively high, corresponding to magnesium biotite in the Mg-($Al^{VI}+Fe^{3+}+Ti$)-(Fe²⁺+Mn) diagram (Fig. 8b). The Mg/(Fe+Mg) ratio increases gradually from the biotite monzogranite (average 0.49) to the monzogranite (0.56), indicating that the biotite became more Mg-rich as the magma evolved.

5. Discussion

5.a. Magmatic evolution

The contents of TiO_2 , Al_2O_3 , FeO, CaO, P_2O_5 and MgO (Fig. 9a–f) decrease with increasing SiO_2 from the biotite monzogranite to the monzogranite, attributed to the separation of some minerals. As previously mentioned, the biotite monzogranite is composed of plagioclase, K-feldspar, quartz, biotite, minor zircon, apatite and magnetite. Among them, biotite in these rocks has high FeO, MgO, Al_2O_3 and TiO_2 (Table S6). Significant fractionation of biotite can cause the variation as observed in Fig. 9. The relatively stable concentration of TiO_2 with decreasing Nb/Ta ratios (Fig. 10a) precludes any major role of magnetite, as the separation of magnetite would lead to a negative correlation between Ti and Nb/Ta (Green & Pearson, 1987; Wang *et al.* 2017). Apatite fractionation was weak during the magmatic evolution, because the P_2O_5 content shows only slight decrease from the biotite monzogranite (average 0.25%) to the monzogranite (average 0.14%). The P_2O_5 also shows decrease with respect to the REE

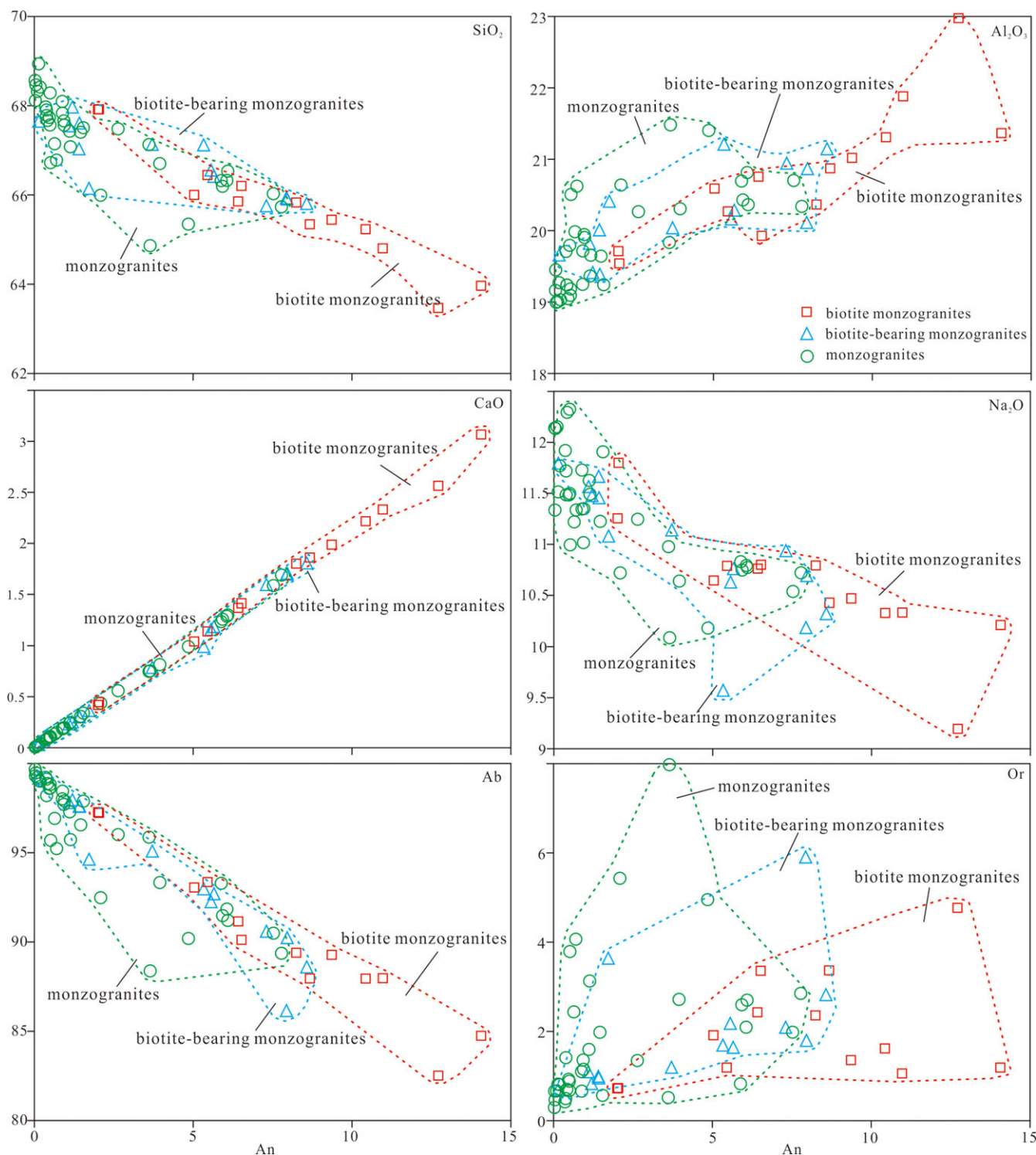


Figure 7. (Colour online) Correlation diagram of plagioclase compositions.

(Fig. 10b). Plagioclase is a major mineral in the monzogranite and has high Al₂O₃, CaO and Na₂O (Table S4). The obvious separation of plagioclase, supported by lower Sr, Eu/Eu* for the monzogranite, the weak decrease in Rb concentrations and decrease of Ba concentrations with decreasing Sr concentrations (Fig. 10c, d), the increasing Rb/Ba and Rb/Sr ratios with decreasing Eu and Ba concentrations (Fig. 10e, f), are also typical. It has been known that fractional crystallization of plagioclase could result in decreasing of

Sr of the residual magma, while the declining Ba is due to the separation of K- feldspar, attributed to the high partition coefficient of Sr for plagioclase and Ba for K- feldspar. The lower Ba (average 1284 ppm) and Sr (average 510 ppm) concentrations for the monzogranite than the biotite monzogranite (average 1637 ppm and 824 ppm, respectively) also indicate fractional crystallization of plagioclase and K- feldspar. Collectively, the BZGs are the products of magmatic evolution, and fractional

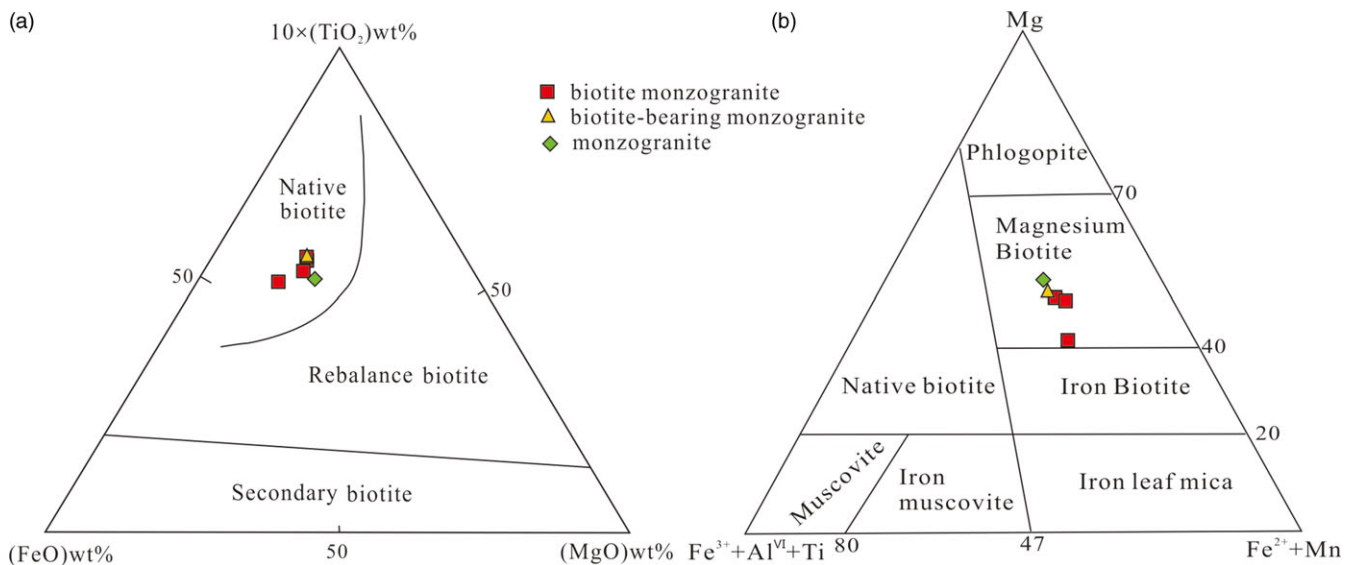


Figure 8. (Colour online) Genesis (a, after Nachit *et al.* 2005) and classification (b, after Foster, 1960) diagram of biotite.

crystallization of biotite, plagioclase, K-feldspar and apatite is the major magmatic process.

5.b. Petrogenetic model

The BZGs have high SiO_2 ($\geq 56\%$), Al_2O_3 ($\geq 14.5\%$) and Sr (> 400 ppm), low Y (< 18 ppm) and Yb (< 1.9 ppm), corresponding with the high Sr/Y (> 35) and La/Yb (> 60) features of characteristics of adakites (Defant & Drummond, 1990; Sajona *et al.* 1993). Also, they plot in the adakite area in the Sr/Y-Y and (La/Yb)_N-Yb_N diagram (Fig. 11). Both of them indicate that our studied rocks have the properties of adakite. Various models have been proposed for the genesis of adakites including: (1) partial melting of a subducting slab (e.g. Kay, 1978; Saunders *et al.* 1987); (2) partial melting of the thickened lower crust (e.g. Yang *et al.* 2016; Xu *et al.* 2018); (3) mixing of mantle-derived and crust-derived magma (e.g. Xu *et al.* 2012; Zhang *et al.* 2013); and (4) fractional crystallization and assimilation (AFC) of mantle-derived basaltic magma (e.g. Chiaradia *et al.* 2004; Macpherson *et al.* 2006; Foley *et al.* 2013; Dai *et al.* 2017; Azizi *et al.* 2019; Temizel *et al.* 2020; Wang *et al.* 2020).

In general, adakites formed by partial melting of the subducted slab are characterized by high Na_2O and low K_2O contents ($\text{Na}_2\text{O} > 3.5\%$, $\text{K}_2\text{O}/\text{Na}_2\text{O} \approx 0.4$) (Richards & Kerrich, 2007), which is not consistent with our samples because $\text{K}_2\text{O}/\text{Na}_2\text{O}$ ratios range from 1.12 to 1.13 (average 1.12), 0.99 to 1.53 (average 1.18) and 0.90 to 1.57 (average 1.12), respectively. As a consequence, partial melting of subducted slab is unlikely. Second, there is no evidence for the required regional crustal uplift in response to the delamination of a thickened lower crust (Li *et al.* 2013). Furthermore, the BZGs are massive and homogeneous, and no direct evidence has been found in the field for magma mixing, such as the presence of mafic enclaves. The limited Sr-Nd isotopic composition variation with ($^{87}\text{Sr}/^{86}\text{Sr}(t)$) ranging from 0.70445 to 0.70524, and $\epsilon\text{Nd}(t)$ from -7.3 to -1.7 (Xiong *et al.* 2017), and the lack of any correlation between Sr-Nd and SiO_2 also precludes the magma mixing model (Li *et al.* 2013).

In summary, we infer that the adakitic BZGs were products of fractional crystallization and assimilation (AFC) of mantle-derived basaltic magma.

5.c. Magmatic physiochemical conditions

5.c.1. Temperature

The distribution of some trace elements in minerals is a function of temperature and is used as a geological thermometer (Albuquerque, 1973). Henry *et al.* (2005) proposed the thermometers for titanium content in biotite: $T = \{[\ln(\text{Ti}) - a - c(X_{\text{Mg}})^3]/b\}^{0.333}$. The procedure follows $T =$ temperature ($^{\circ}\text{C}$); Ti = the number of Ti cations in biotite based on 22 oxygen atoms, calculated using the Luhr method (Luhr *et al.* 1984); $X_{\text{Mg}} = \text{Mg}/(\text{Mg} + \text{Fe})$; $a = -2.3594$, $b = 4.6484 \times 10^{-9}$, $c = -1.7283$. The calculation results are listed in Supplementary Table S8, indicating that the crystallization temperature of the biotite ranges from 700°C to 744°C (average 723°C). Besides, zircon crystallization temperatures of biotite-bearing monzogranite and monzogranite were estimated using the equations of Weston *et al.* (2006): $[\log_{10}\text{Ti in zircon (ppm)}] = (6.01 \pm 0.03) - (5080 \pm 30)/T(\text{K})$, listed in Table S2. The biotite-bearing monzogranite shows zircon temperature in the range of 679 – 732°C ($n = 15$, average 705°C). The zircon temperatures of monzogranite are relatively concentrated (except for the -30 – 7 – 6 of 783°C), ranging from 693 to 727°C ($n = 14$, average 709°C), suggesting that they have similar high crystallization temperature. Both estimates are consistent with the features shown by the biotite, indicating that the BZGs were formed at a temperature of ca. 700°C .

5.c.2. Pressure

The Al content of biotite is positively correlated with the pressure of granitoids according to Uchida *et al.* (2007). They proposed the empirical formula: $P(\text{kbar}) = 3.03 \times T^{\text{Al}} - 6.53$ (± 0.33) (T^{Al} = the number of Al cations in biotite based on 22 oxygen atoms, calculated using the Luhr method) (Luhr *et al.* 1984). The results show that the BZG emplacement pressure is between 0.71 kbar and 1.60 kbar (average 0.97 kbar), corresponding to paleodepths of 2.7 to 6.0 km under lithostatic pressure.

5.c.3. Oxygen fugacity

The concentration of Fe^{3+} , Fe^{2+} , Mg^{2+} in biotite can be used to estimate $f\text{O}_2$ (e.g. Dymek, 1983; Wones, 1989). The Fe^{2+} - Fe^{3+} - Mg^{2+} ternary diagram (Fig. 12) shows that the biotite from BZGs

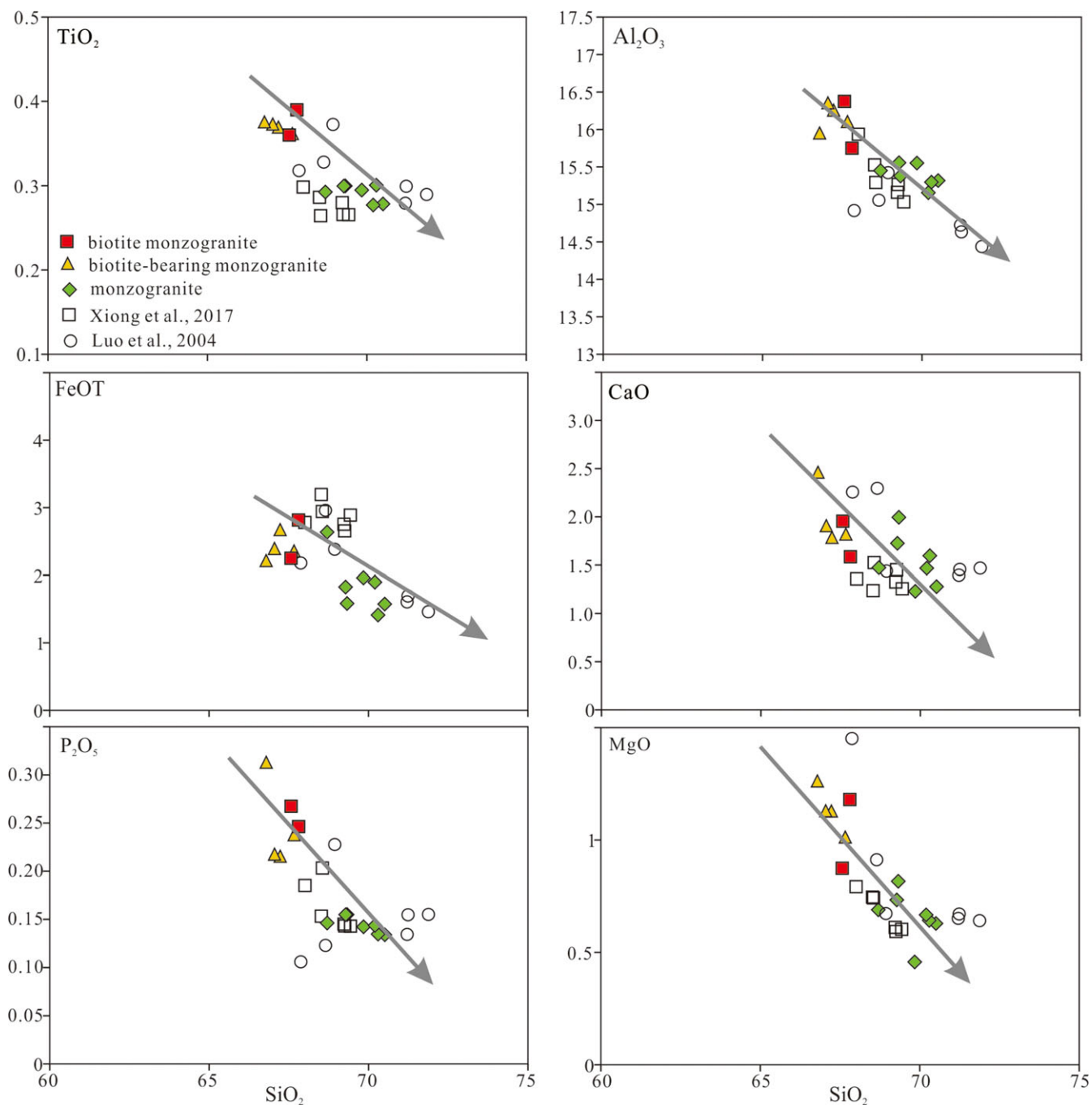


Figure 9. (Colour online) Variation of $\omega(\text{SiO}_2)$ % vs. $\omega(\text{TiO}_2)$ %, $\omega(\text{Al}_2\text{O}_3)$ %, $\omega(\text{FeO}_7)$ %, $\omega(\text{CaO})$ %, $\omega(\text{P}_2\text{O}_5)$ %, $\omega(\text{MgO})$ %.

plot in the compositional fields between the Ni-NiO and Fe_2O_3 - Fe_3O_4 buffer, and closer to Fe_2O_3 - Fe_3O_4 line, indicating a high $f\text{O}_2$ in the environment of biotite crystallization from the BZGs parent magma. Moreover, zircon $f\text{O}_2$ was calculated using the Ti in zircon of Geo- $f\text{O}_2$ software (Li *et al.* 2019), listed in Table S2. $\log f\text{O}_2$, ΔFMQ , and ΔNNO for the biotite-bearing monzogranite vary from -22.39 to -13.44 (average of -17.02), -6.31 to $+1.30$ (average of -1.67), and -6.88 to $+0.74$ (average of -2.22), respectively. The monzogranite shows higher values of $\log f\text{O}_2$, ΔFMQ and ΔNNO , ranging from -19.76 to -11.71 (average of -15.14), -4.93 to $+3.67$ (average of -0.03) and -5.48 to $+3.11$ (average of -0.58), respectively. These data suggest that the magma

may have evolved to a more oxidized state from the biotite-bearing monzogranite to monzogranite.

5.d. Potential link between magmatism and mineralization

5.d.1. Conductive factors

Fractional crystallization is considered to be a critical component for mineralization (e.g. Blevin, 2004; Chiaradia *et al.* 2012; Hronsky *et al.* 2012). As discussed in previous sections, fractional crystallization played a dominant role during magma differentiation of the BZGs.

Besides, other three parameters have been proposed to evaluate the magmatic-hydrothermal associated with gold-bearing

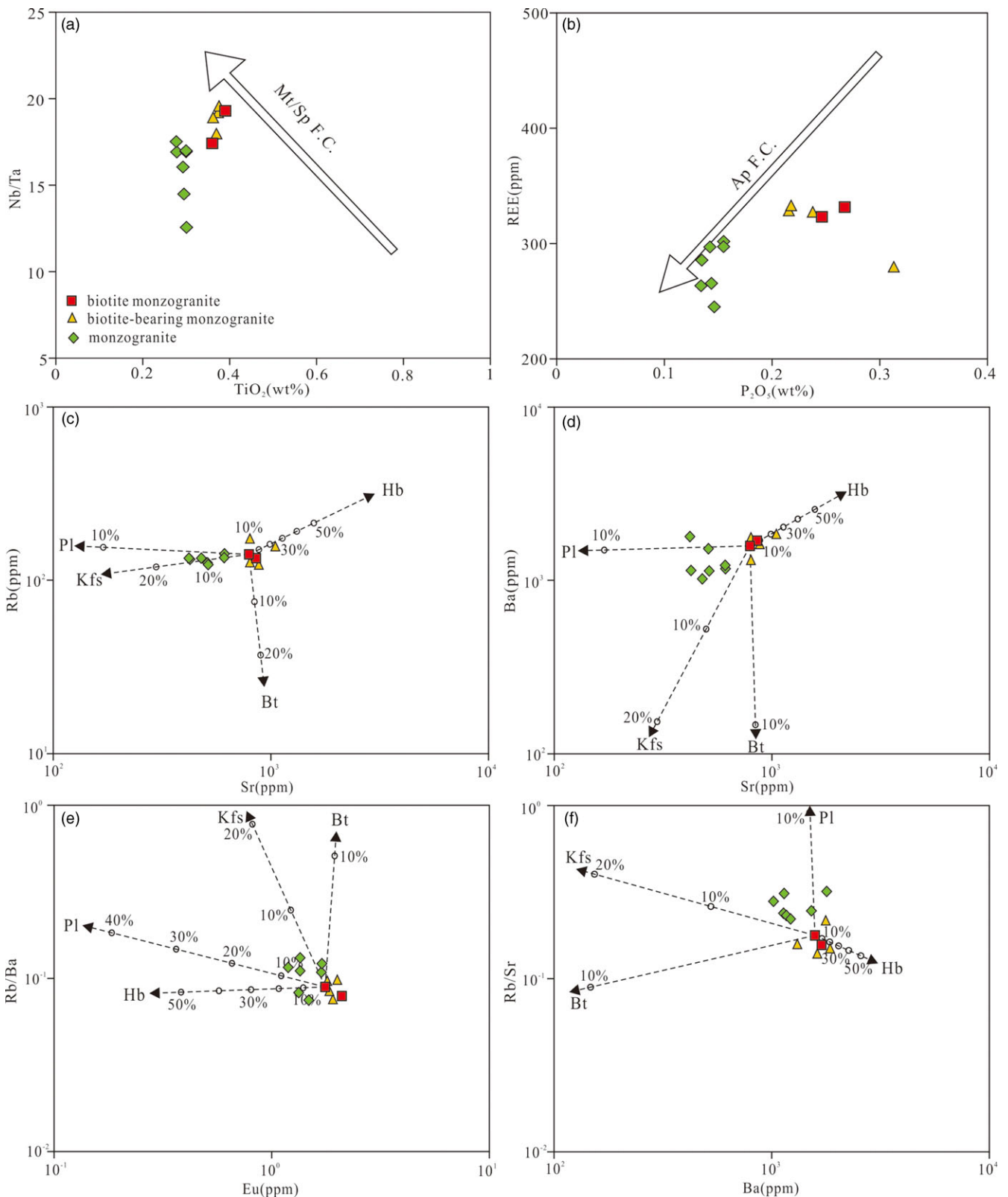


Figure 10. (Colour online) Diagrams of (a) TiO₂ (wt%) versus Nb/Ta ratios, (b) P₂O₅ (wt%) versus REE (ppm) (after Wang *et al.* 2017), (c) Sr (ppm) versus Rb (ppm), (d) Sr (ppm) versus Ba (ppm), (e) Eu (ppm) versus Rb/Ba ratios and (f) Ba (ppm) versus Rb/Sr ratios, showing the fractional crystallization of different minerals. See Supplementary Table S7 for the partition of those minerals. Symbols are: Mt = magnetite; Sp = spinel; Hb = hornblende; Pl = plagioclase; Kf = K-feldspar; Bt = biotite; Ap = apatite.

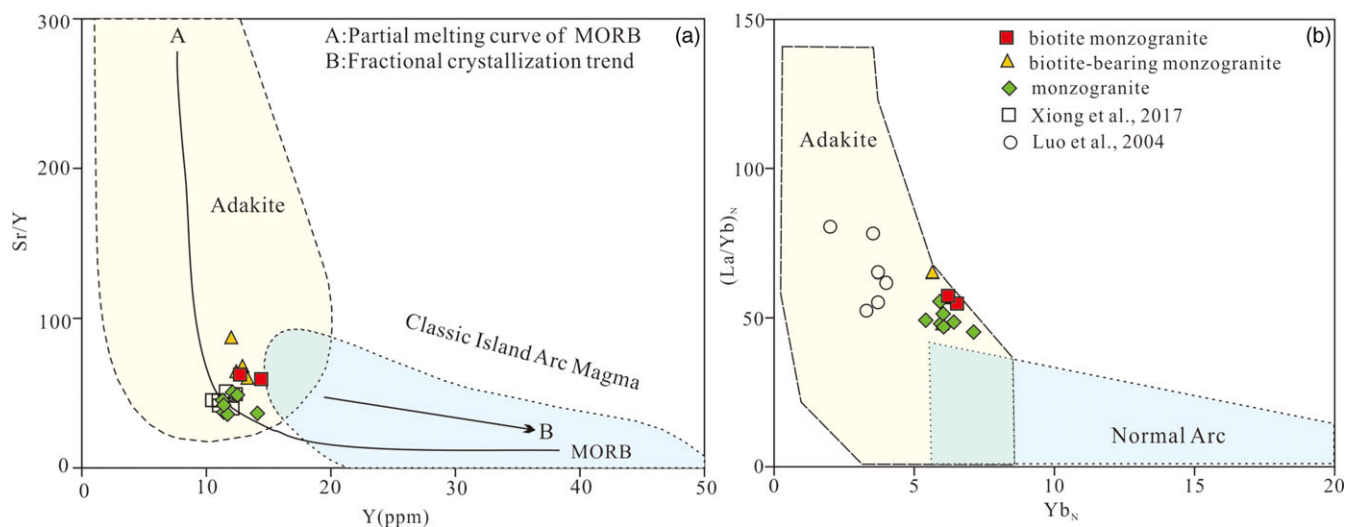


Figure 11. (Colour online) (a) Variation of Sr/Y vs. Y. Fields for adakites and island arcs are from Defant and Drummond (1990). (b) Variation of $(La/Yb)_N$ vs. Yb_N . Data are normalized (N) to C1 (chondrite) values of Sun & McDonough (1989). Fields for adakites and island arc magma are from Martin (1999).

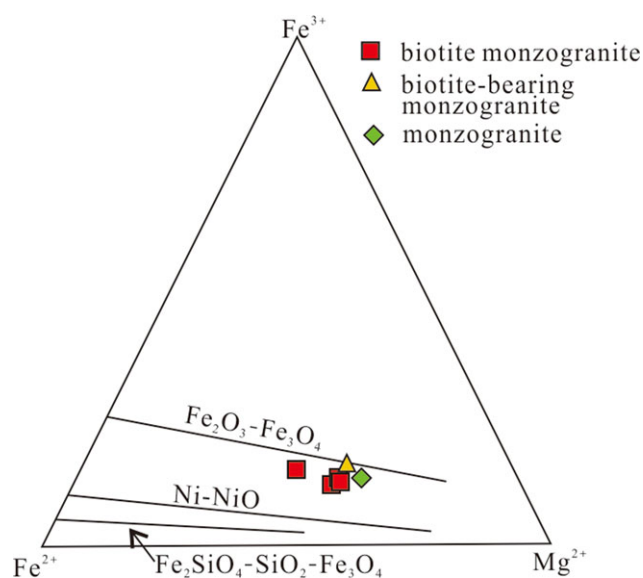


Figure 12. (Colour online) Fe^{2+} - Fe^{3+} - Mg^{2+} ternary diagram (after Wones, 1989) of the biotite from the BZGs.

granitoids by Blevin (2004): (1) redox state; (2) compositions, for example, K_2O and alkalinity; (3) degree of magma evolution.

On the redox state classification diagram of Fe^{2+} - Fe^{3+} - Mg^{2+} (Fig. 12), the studied rocks are closer to Fe_2O_3 - Fe_3O_4 , indicating that they belong to the magnetite series. The magnetite-bearing granitoids are generally related to Au, Cu and Mo deposits (Ishihara, 1977). Furthermore, the BZGs have a high fO_2 , as evidenced by EPMA data of biotite and trace element characteristics of zircon, which are favourable for gold mineralization (Park *et al.* 2015; Xu *et al.* 2021).

The BZGs are alkali-rich, with $Na_2O + K_2O$ values ranging from 9.77 to 9.99% (average 9.88%), 9.93 to 10.16% (average 10.07%), 9.87 to 10.25% (average 10.07%), respectively. On the $(Na_2O+K_2O - CaO)$ versus SiO_2 diagram, they all plot as alkaline series (Fig. 5c). On the other hand, potassium alteration is also observed (Fig. 2h), which is a significant feature of gold deposits

related to alkaline magmatism (Jensen & Barton, 2000), and is favourable for the transport of gold (N'dri *et al.* 2021).

The Rb/Sr and K/Rb ratios are two useful parameters to evaluate the degree of compositional evolution. The Rb/Sr ratio of the studied rocks is low (0.16–0.18, 0.14–0.22 and 0.22–0.32, respectively), indicating that these rocks are less evolved (Blevin, 2004). Previously studied Au-Cu deposits are related to low differentiation granites (Thompson *et al.* 1999; Blevin *et al.* 2003). In addition, granites associated with Cu and Cu-Au deposits have a K/Rb ratio >200 (Blevin, 2004). The K/Rb ratio is all greater than 200 of the BZGs, ranging from 296 to 318 (average 307), 275 to 326 (average 301) and 306 to 350 (average 324), respectively. The above features suggest that the BZGs are less evolved and conducive to gold mineralization according to Blevin (2004).

5.d.2. Timing of magmatism and gold mineralization

The northern margin of the NCC is an important gold mineralization belt, and there are multiple magmatic events associated with numerous gold mineralization (e.g. N'dri *et al.* 2021). These gold ores are hosted by both Precambrian metamorphic rocks and Variscan, Indosinian and Yanshanian granites (Zhou *et al.* 2002). Many gold deposits, related to the Mesozoic intrusive rocks, are distributed in the eastern Hebei – western Liaoning area in the northern margin of the NCC (Kong *et al.* 2015). These deposits have almost the same mineralization age as that of magmatism (Chen *et al.* 2019; Zhang *et al.* 2020), such as Yuerya and Jinchangyu (Wang *et al.* 2020).

In this study, the zircon U-Pb dates of 231.7 ± 3.6 Ma (biotite-bearing monzogranite sample 0–8) and 231.7 ± 3.3 Ma (monzogranite sample -30-7) have been obtained from the BZGs. They are very similar to those reported previously, where LA-ICP-MS zircon U-Pb ages show 233 ± 3 Ma (Xiong *et al.* 2017) and SHRIMP zircon U-Pb ages yielded 222 ± 3 Ma (Luo *et al.* 2004). All these data indicate that the time of magmatism is Late Triassic. We therefore speculate that the Baizhangzi gold deposit, one of the typical IRGDs, was also formed in the Late Triassic. It was also demonstrated by a number of investigated gold deposits hosted by igneous rocks, including Bilihe (Yang *et al.* 2016), Daxiyingzi (Liu *et al.* 2021), Julia (Soloviev *et al.* 2022) and Xiajinbao (Wang *et al.* 2020).

In summary, the BZGs experienced fractional crystallization, together with high fO_2 , alkali-rich, K-metasomatism and low evolution degree, which are conducive for gold mineralization. Furthermore, the monzogranite probably has high metallogenic potential due to its more oxidized state. We expect that this investigation will provide an important guide for regional gold exploration in the area.

6. Conclusions

- (1) Zircon U–Pb dating shows that the biotite-bearing monzogranite and monzogranite were formed at 231.7 ± 3.6 Ma and 231.7 ± 3.3 Ma, respectively. The dating, supporting previous geochronology, represents the age of magmatism and gold mineralization in the area.
- (2) Bulk and mineral geochemistry data indicate that the BZGs are cogenetic and fractional crystallization is the dominant magmatic process.
- (3) Crystallization temperature is ca. 700°C, and pressure is between 0.71 kb and 1.60 kb of the BZGs. Zircon trace elements suggest that the magma may have evolved to a more oxidized state.
- (4) The fractional crystallization, together with high fO_2 , K-metasomatism and low evolution degree, are considered favourable conditions for gold mineralization.

Supplementary material. The supplementary material for this article can be found at <https://doi.org/10.1017/S0016756823000341>

Acknowledgements. This research was financially supported by the Natural Science Foundation of China (grant No. 92062217 and 42121002). We thank Xiaohong Mao of the Institute of Geology, Chinese Academy of Geological Science for the assistance in geochemical and isotope analysis.

Competing interests. The authors declare that all authors have contributed to this manuscript, and they have no known competing financial interests or personal relationships that could have appeared to influence the work reported in this paper.

References

- Albuquerque CAR (1973) Geochemistry of biotite from granitic rocks, northern Portugal. *Geochemical et Cosmochimica Acta* **37**, 1779–802.
- Andersen T (2002) Correction of common lead in U–Pb analyses that do not report ^{204}Pb . *Chemical Geology* **192**, 59–79.
- Azizi H, Stern RJ, Topuz G, Asahara Y and Moghadam HS (2019) Late Paleocene adakitic granitoid from NW Iran and comparison with adakites in the NE Turkey: Adakitic melt generation in normal continental crust. *Lithos* **346–347**, e105151. doi: [10.1016/j.lithos.2019.105151](https://doi.org/10.1016/j.lithos.2019.105151).
- Bai Y, Zhu MT, Zhang LC, Huang K and Li WJ (2019) Auriferous pyrite Re–Os geochronology and He–Ar isotopic compositions of the Jinchangyu Au deposit in the northern margin of the North China Craton. *Ore Geology Reviews* **111**, e102948. doi: [10.1016/j.oregeorev.2019.102948](https://doi.org/10.1016/j.oregeorev.2019.102948).
- Barker F and Millard HT (1979) Geochemistry of the type Trondhjemite and three associated rocks, Norway. *Developments in Petrology* **6**, 517–29.
- Blevin PL (2004) Redox and compositional parameters for interpreting the granitoid metallogeny of Eastern Australia: implications for good-rich ore systems. *Resource Geology* **54**, 241–52.
- Blevin PL, Chappell BW and Jones M (2003) Magmas to mineralisation: the Ishihara Symposium. *Abstract volume GEMOC*, Macquarie University, July 22–24.
- Cepedal A, Fuertes-Fuente M, Martín-Izard A, García-Nieto J and Boiron MC (2013) An intrusion-related gold deposit (IRGD) in the NW of Spain, the Linares deposit: igneous rocks, veins and related alterations, ore features and fluids involved. *Journal of Geochemical Exploration* **124**, 101–26.
- Chen SC, Ye HT, Wang YT, He W, Zhang XK and Wang NN (2019) ^{40}Ar – ^{39}Ar age of altered sericite from Yuerya Au deposit in eastern Hebei Province and its geological significance. *Mineral Deposits* **38**, 557–70 (in Chinese with English abstract).
- Chen SC, Ye HT, Wang YT, Zhang XK, Lu DY and Hu HB (2014) Re–Os age of molybdenite from the Yuerya Au deposit in eastern Hebei Province and its geological significance. *Geology in China* **41**, 1565–76 (in Chinese with English abstract).
- Chiaradia M, Fontboté L and Beate B (2004) Cenozoic continental arc magmatism and associated mineralization in Ecuador. *Mineralium Deposita* **39**, 204–22.
- Chiaradia M, Ulianov A, Kouzmanov K and Beate B (2012) Why large porphyry Cu deposits like high Sr/Y magmas. *Scientific Reports* **2**, 1–5.
- Christopher MF, Keith NS and Robert HR (2003) Detrital zircon analysis of the sedimentary record. *Mineralogy and Geochemistry* **53**, 277–303.
- Cox A, Dabiche MG and Engebretson DC (1989) Terrane trajectories and plate interactions along continental margins in the north Pacific basin. In *The Evolution of the Pacific Ocean Margins*, (ed Z. Ben-Avraham), pp. 20–35. New York, NY, Oxford University Press.
- Dai HK, Zheng JP, Zhou X and Griffin WL (2017) Generation of continental adakitic rocks: crystallization modeling with variable bulk partition coefficients. *Lithos* **272–273**, 222–31.
- Davis GA, Zheng YD, Wang C, Darby BJ, Zhang C and Gehrels G (2001) Mesozoic tectonic evolution of the Yanshan fold and thrust belt, with emphasis on Hebei and Liaoning provinces, northern China. In: Hendrix, M.S., Davis, G.A. (Eds.), *Paleozoic and Mesozoic Tectonic Evolution of Central Asia: from Continental Assembly to Intracontinental Deformation*. *Geological Society of America Memoir* **194**, 171–97.
- Defant MJ and Drummond MS (1990) Derivation of some modern arc magmas by melting of young subducted lithosphere. *Nature* **347**, 662–5.
- Deng J and Wang Q (2016) Gold mineralization in China: metallogenic provinces, deposit types and tectonic framework. *Gondwana Research* **36**, 219–74.
- Dressel BC, Chauvet A, Trzaskos B, Biondi JC, Bruguier O, Monié P, Villanova SN and Newton JB (2018) The Passa Três lode gold deposit (Paraná State, Brazil): an example of structurally-controlled mineralisation formed during magmatic-hydrothermal transition and hosted within granite. *Ore Geology Reviews* **102**, 701–27.
- Dymek RF (1983) Titanium, aluminum and interlayer cation substitutions in biotite from high-grade gneisses, West Greenland. *American Mineralogist* **68**, 880–99.
- Foley FV, Pearson NJ, Rushmer T, Turner S and Adam J (2013) Magmatic evolution and magma mixing of quaternary Adakites at Solander and Little Solander Islands, New Zealand. *Journal of Petrology* **54**, 703–44.
- Foster MD (1960) Interpretation of the composition of trioctahedral micas. *US Geological Survey Professor Paper* **354B**, 1–49.
- Frost BR, Barnes CG, Collins WJ, Arculus RJ, Ellis DJ and Frost CD (2001) A geochemical classification for granitic rocks. *Journal of Petrology* **43**, 2033–48.
- Goldfarb RJ and Groves DI (2011) Orogenic gold: common or evolving fluid and metal sources through time. *Lithos* **233**, 2–26.
- Goldfarb RJ, Groves DI and Gardoll S (2001) Orogenic gold and geologic time: a global synthesis. *Ore Geology Reviews* **18**, 1–75.
- Green TH and Pearson NJ (1987) An experimental study of Nb and Ta partitioning between Ti-rich minerals and silicate liquids at high pressure and temperature. *Geochimica et Cosmochimica Acta* **51**, 55–62.
- Groves DI and Santosh M (2016) The giant Jiaodong gold province: the key to a unified model for orogenic gold deposits?. *Geoscience Frontiers* **7**, 409–17.
- Henry DJ, Guidotti CV and Thomson JA (2005) The Ti-saturation surface for low- to- medium pressure metapelitic biotite: implications for geothermometry and Ti-substitution mechanisms. *Journal of American Mineralogist* **90**, 316–28.
- Hoskin PWO and Ireland TR (2000) Rare earth element chemistry of zircon and its use as a provenance indicator. *Geology* **28**, 627–30.
- Hronsky JM, Groves DI, Loucks RR and Begg GC (2012) A unified model for gold mineralization in accretionary orogens and implications for regional-scale exploration targeting methods. *Mineralium Deposita* **47**, 339–58.

- Ishihara SI (1977) The magnetite-series and Ilmenite-series Granitic Rocks. *Mining Geology* **27**, 293–305.
- Jan K and Sylvester PJ (2003) Present trends and the future of zircon in geochronology: laser ablation ICPMS. *Mineralogy and Geochemistry* **53**, 243–75.
- Jensen EP and Barton M (2000) Gold deposits related to alkaline magmatism. *Reviews in Economic Geology* **13**, 279–314.
- Jiang N, Guo JH and Chang GH (2013) Nature and evolution of the lower crust in the eastern North China craton: a review. *Earth Science Reviews* **122**, 1–9.
- Jiang SH, Bagas L, Liu YF and Zhang LL (2018) Geochronology and petrogenesis of the granites in Malanyu Anticline in eastern North China Block. *Lithos* **312**, 21–37.
- Kay RW (1978) Aleutian magesian andesites: melts from subducted Pacific Ocean crust. *Journal of Volcanology and Geothermal Research* **4**, 117–32.
- Kong DX, Xu JF, Yin JW, Chen JL, Li J, Guo Y, Yang HT and Shao XK (2015) Electron microprobe analyses of ore minerals and H–O, S isotope geochemistry of the Yuerya gold deposit, eastern Hebei, China: implications for ore genesis and mineralization. *Ore Geology Reviews* **69**, 199–216.
- Lang JR and Baker T (2001) Intrusion-related gold systems: the present level of understanding. *Mineralium Deposita* **36**, 477–89.
- Le Maitre RW (2002) *Igneous Rocks: A Classification and Glossary of Terms Second*. Cambridge, UK: Cambridge University Press, pp. 1–236.
- Leal S, Lima A, Morris J, Pedro M and Noronha F (2022) Numão gold deposit in the Iberian Variscan belt, Northern Portugal: ore features and mineralization controls. A gold deposit in a W–Sn metallogenic province. *Ore Geology Reviews* **144**, e104815. doi: [10.1016/j.oregeorev.2022.104815](https://doi.org/10.1016/j.oregeorev.2022.104815).
- Li H, Li YJ, Xu XY, Yang GX, Wang ZP, Xu Q and Ning WT (2020) Geochemistry, petrogenesis and geological significance of Early Carboniferous adakite in Sawuer region, West Junggar, Xinjiang. *Acta Petrologica Sinica* **36**, 2017–34 (in Chinese with English abstract).
- Li WK, Cheng YQ and Yang ZM (2019) Geo- fO_2 : Integrated software for analysis of magmatic oxygen fugacity. *Geochemistry, Geophysics, Geosystems* **20**, 2542–55.
- Li X, Zhang C, Behrens H and Holtz F (2020) Calculating biotite formula from electron microprobe analysis data using a machine learning method based on principal components regression. *Lithos* **356–357**. doi: [10.1016/j.lithos.2020.105371](https://doi.org/10.1016/j.lithos.2020.105371).
- Li XH, Li ZX, Li WX, Wang XC and Gao YY (2013) Revisiting the “C-type adakites” of the Lower Yangtze River Belt, central eastern China: in-situ zircon Hf–O isotope and geochemical constraints. *Chemical Geology* **345**: 1–15.
- Liu CF, Zhao SH and Liu WC (2021) The relationship between gold mineralization, high K calc-alkaline to alkaline volcanic rocks, and A-type granite: formation of the Daxiyingzi gold deposit in northern North China Craton. *Ore Geology Reviews* **138**, 104383. doi: [10.1016/j.oregeorev.2021.104383](https://doi.org/10.1016/j.oregeorev.2021.104383).
- Liu J, He JC, Lai CK, Wang XT and Li TG (2022) Time and Hf isotopic mapping of Mesozoic igneous rocks in the Argun massif, NE China: implication for crustal architecture and its control on polymetallic mineralization. *Ore Geology Reviews* **141**, 104648. doi: [10.1016/j.oregeorev.2021.104648](https://doi.org/10.1016/j.oregeorev.2021.104648).
- Liu SA, Li S, Guo S, Hou Z and He Y (2012) The Cretaceous adakitic–basaltic–granitic magma sequence on south-eastern margin of the North China Craton: implications for lithospheric thinning mechanism. *Lithos* **134–135**, 163–78.
- Liu YS, Hu ZC, Zong KQ, Gao CG and Chen CC (2010) Reappraisal and refinement of zircon U–Pb isotope and trace element analyses by LA-ICP-MS. *Chinese Science Bulletin* **55**, 1535–46.
- Lu SN, Zhao GC, Wang HC and Hao GJ (2008) Precambrian metamorphic basement and sedimentary cover of the North China Craton: a review. *Precambrian Reviews* **160**, 77–93.
- Ludwig KR (2003) *User's Manual for Isoplot v. 3.00: A Geochronological Toolkit for Microsoft Excel*. Berkeley, CA: Berkeley Geochronology Center, pp. 60–61.
- Luhr JF, Carmichael ISE and Varekamp JC (1984) The 1982 eruptions of El Chichón volcano, Chiapas, Mexico: Mineralogy and petrology of the anhydrite phenocryst-bearing pumices. *Journal of Volcanology & Geothermal Research*, **23**, 69–108.
- Luo ZK, Guan K, Qiu YS and Miao LC (2001) Zircon SHRIMP U–Pb dating of albite dyke in Jinchangyu gold mine, Jidong area, Hebei, China. *Geological Prospecting Theory Cluster* **16**, 226–31 (in Chinese with English abstract).
- Luo ZK, Li JJ, Guan K, Qiu YS, Qiu YM, McNaughton NJ and Groves DI (2004) SHRIMP zircon U–Pb age of the granite at Baizhangzi gold field in Lingyuan, Liaoning Province. *Geological Survey and Research* **27**, 82–5 (in Chinese with English abstract).
- Luo ZK, Miao LC, Guan K, Qiu YS, Qiu YM, McNaughton NJ and Groves DI (2003) SHRIMP U–Pb zircon dating of the Dushan granitic batholith and related granite-porphry dyke, eastern Hebei Province, China, and their geological significance. *Geochemica* **32**, 173–80 (in Chinese with English abstract).
- Macpherson CG, Dreher ST and Thirwall MF (2006) Adakites without slab melting: high pressure processing of basaltic island arc magma, indanao, the Philippines. *Earth and Planetary Science Letters* **243**, 581–93.
- Manilar PD and Piccoli PM (1989) Tectonic discrimination of granitoids. *Geological Society of America Bulletin* **101**, 635–43.
- Martin H (1999) Adakitic magmas: modern analogues of Archaean granitoids. *Lithos* **46**, 411–29.
- Miao L, Qiu Y, Fan W and Zhang F (2008) Mesozoic multi-phase magmatism and gold mineralization in the early Precambrian North China craton, eastern Hebei Province, China: SHRIMP zircon U–Pb evidence. *International Geology Review* **50**, 826–47.
- Miao LC, Qiu YM, Fan WM, Zhang FQ and Zhai MG (2005) Geology, geochronology, and tectonic setting of the Jiapigou gold deposits, southern Jilin Province, China. *Ore Geology Reviews* **26**, 137–65.
- N'dri KA, Zhang DH, Zhang T, Tamehe LS, Kouamelan KS, Wu MQ, Assie KR, Koua KAD, Kouamelan AN and Zhang JL (2021) Gold mineralization in the northern margin of the North China Craton: influence of alkaline magmatism and regional tectonic during Middle Paleozoic–Mesozoic. *Ore Geology Reviews* **133**, e103969. doi: [10.1016/j.oregeorev.2020.103969](https://doi.org/10.1016/j.oregeorev.2020.103969).
- Nachit H, Ibhi A, Abia EH and Ohoud MB (2005) Discrimination between primary magmatic biotites, re-equilibrated biotites and neofomed biotites. *Comptes Rendus Geoscience* **337**, 1415–20.
- Nie FJ, Jiang SH and Liu Y (2004) Intrusion-related gold deposits of North China Craton, People's Republic of China. *Resource Geology* **54**, 299–324.
- Park JW, Campbell LH, Kim J and Moon JW (2015) The role of late sulfide saturation in the formation of a Cu and Au-rich magma: insights from the platinum group element geochemistry of Niutahi-Motutahi Lavas, Tonga Rear Arc. *Journal of Petrology* **56**, 59–81.
- Randall RP and Stephen RN (2003) Zircon U–Th–Pb Geochronology by isotope dilution—thermal ionization mass spectrometry. *Mineralogy and Geochemistry* **53**, 183–213.
- Rao YX (2002) Discussion on some problems related with granite in east section of Yanshan area. *Mineral Resources and Geology* **16**, 327–31 (in Chinese with English abstract).
- Richards JR and Kerrich R (2007) Special paper: adakite-like rocks: their diverse origins and questionable role in metallogenesis. *Economic Geology* **102**, 537–76.
- Sajona FG, Maury RC, Bellon H, Cotten J, Defant MJ, Pubellier M and Rangin C (1993) Initiation of subduction and the generation of slab melts in western and eastern Mindanao, Philippines. *Geology* **21**, 1007–10.
- Santosh M and Groves DI (2022) Global metallogeny in relation to secular evolution of the earth and supercontinent cycles. *Gondwana Research* **107**, 395–422.
- Saunders AD, Rogers G, Marriner GF, Terrell DJ and Verma SP (1987) Geochemistry of Cenozoic volcanic rocks, Baja California, Mexico: implications for the petrogenesis of post-subduction magmas. *Journal of Volcanology and Geothermal Resource* **32**, 223–45.
- Sillitoe RH and Thompson JFH (1998) Intrusion-related vein gold deposits: types, tectono-magmatic settings, and difficulties of distinction from orogenic gold deposits. *Resource Geology* **48**, 237–50.
- Smith JV (1974) *Feldspar Minerals*. New York: Springer Verlag, pp. 112–45.

- Soloviev SG, Kryazhev SG, Semenova DV, Kalinin YA, Dvurechenskaya SS and Sidorova NV (2022) Geology, mineralization, igneous geochemistry, and zircon U-Pb geochronology of the early Paleozoic shoshonite-related Julia skarn deposit, SW Siberia, Russia: toward a diversity of Cu-Au-Mo skarn to porphyry mineralization in the Altai-Sayan orogenic system. *Ore Geology Reviews* **142**, e104706. doi: [10.1016/j.oregeorev.2022.104706](https://doi.org/10.1016/j.oregeorev.2022.104706).
- Song Y, Jiang SH, Bagas L, Li C, Hu JZ, Zhang Q, Zhou W and Ding HY (2016) The geology and geochemistry of Jinchangyu gold deposit, North China Craton: implications for metallogenesis and geodynamic setting. *Ore Geology Reviews* **73**, 313–29.
- Stone D (2000) Temperature and pressure variations in suites of Archean felsic plutonic rocks, Berensriver area, northwest Superior province, Ontario, Canada. *The Canadian Mineralogist* **38**, 455–70.
- Sun SS and Donough WF (1989) Chemical and isotopic systematics of ocean basalts: implications for mantle composition and process. In *Magmatism in Ocean Basins* (eds AD Saunders and MJ Norry), pp. 313–45. London: Geological Society Special Publication, no. 42.
- Temizel I, Arslan M, Yücel C, Yazar EA, Kaygusuz A and Aslan Z (2020) Eocene tonalite-granodiorite from the Havza (Samsun) area, northern Turkey: adakite-like melts of lithospheric mantle and crust generated in a post-collisional setting. *International Geology Review* **62**, 1131–58.
- Thompson JFH, Sillitoe RH, Baker T, Lang JR and Mortensen JK (1999) Intrusion-related gold deposits associated with tungsten-tin provinces. *Mineralium Deposita* **34**, 323–34.
- Tuduri J, Chauvet A, Barbanson L, Labriki M, Dubois M, Trapy PH, Lahfid A, Poujol M, Melleton J, Badra L, Ennaciri A and Maacha L (2018) Structural control, magmatic-hydrothermal evolution and formation of hornfels-hosted, intrusion-related gold deposits: insight from the Thaghassa deposit in Eastern Anti-Atlas, Morocco. *Ore Geology Reviews* **97**, 171–98.
- Uchida E, Endo S and Makino M (2007) Relationship between solidification depth of granitic rocks and formation of hydrothermal ore deposits. *Resource Geology* **57**, 47–56.
- Wang C (2018) Study on geological characteristics and metallogenic prognosis of BaiZhangZi gold deposit. *Mineral Resources* **12**, 136–7 (in Chinese with English abstract).
- Wang HQ, Gao WS, Deng XD and Li JW (2020) Zircon U-Pb dating reveals Late Jurassic gold mineralization in the Jidong district of the northern North China Craton. *Ore Geology Reviews* **126**, 103798. doi: [10.1016/j.oregeorev.2020.103798](https://doi.org/10.1016/j.oregeorev.2020.103798).
- Wang QD (1989) Research on the mechanism of the transportation and precipitation of gold in Baizhangzi gold deposit. *Mining and geology* **3**, 49–53 (in Chinese with English abstract).
- Wang YJ, Wang XS, Bi XW, Tao Y and Lan TG (2020) Intraplate adakite-like rocks formed by differentiation of mantle-derived mafic magmas: a case study of Eocene intermediate-felsic porphyries in the Machangqing porphyry Cu-Au mining district, SE Tibetan plateau. *Journal of Asian Earth Sciences* **196**, e104364. doi: [10.1016/j.jseae.2020.104364](https://doi.org/10.1016/j.jseae.2020.104364).
- Wang YY, Zeng LS, Chen FK, Cai JH, Yan GH, Hou KJ and Wang Q (2017) The evolution of high Ba-Sr granitoid magmatism from “crust-mantle” interaction: a record from the Laoshan and Huyanshan complexes in the central North China Craton. *Acta Petrologica Sinica* **33**, 3873–96 (in Chinese with English abstract).
- Watson EB, Wark DA and Thomas JB (2006) Crystallization thermometers for zircon and rutile. *Contributions to Mineralogy & Petrology* **151**, 413–33.
- Wei Q, Xuan L, Ma L, Diao WY, Liu ZM, Zheng YX, Guo TC and Zhang JF (2016) Prospecting new progress and significance in Maojiadian-Baizhangzi gold-concentrated area. *Non-ferrous Mining and Metallurgy* **32**, 4–9 (in Chinese with English abstract).
- Wilde SA, Zhao GC and Sun M (2002) Development of the North China Craton during the Late Archaean and its final amalgamation at 1.8 Ga; some speculations on its position within a global Palaeoproterozoic supercontinent. *Gondwana Research* **5**, 85–94.
- Wones DR (1989) Significance of the assemblage titanite + magnetite + quartz in granitic rocks. *American Mineralogist* **74**, 744–9.
- Wu FY, Han RH, Yang JH, Wilde SA and Zhai MG (2007) Initial constraints on the timing of granitic magmatism in North Korea using U-Pb zircon geochronology. *Chemical Geology* **238**, 232–48.
- Wu FY, Lin JQ, Wilde SA, Zhang XO and Yang JH (2005b) Nature and significance of the early Cretaceous giant igneous event in Eastern China. *Earth and Planetary Science Letters* **233**, 103–19.
- Wu FY, Sun DY, Ge WC, Zhang YB, Grant ML, Wilde SA and Jahn BM (2011) Geochronology of the Phanerozoic granitoids in northeastern China. *Journal of Asian Earth Sciences* **41**, 1–30.
- Wu FY, Yang JH and Liu XM (2005a) Geochronological framework of the Mesozoic granitic magmatism in the Liaodong Peninsula, Northeast China. *Geological Journal of China Universities* **11**, 305–17 (in Chinese with English abstract).
- Xiong L, Shi WJ, Li H, Tian N, Chen C, Zhou HZ, Zhao SQ and Li PY (2017) Geochemistry, Sr-Nd-Hf isotopes and petrogenesis of Mid-Late Triassic Baizhangzi granitic intrusive rocks in eastern Hebei-western Liaoning province. *Earth Science* **42**, 207–22 (in Chinese with English abstract).
- Xu DR, Wang ZL, Wu CJ, Zhou YQ, Shan Q, Hou MZ, Fu YR and Zhang XW (2017) Mesozoic gold mineralization in Hainan Province of South China: genetic types, geological characteristics and geodynamic settings. *Journal of Asian Earth Sciences* **137**, 80–108.
- Xu HJ, Ma CQ and Zhang JF (2012) Generation of early Cretaceous high-Mg adakitic host and enclaves by magma mixing, Dabie orogen, Eastern China. *Lithos* **142–143**, 182–200.
- Xu JC, Gu XX, Wang JL, Zhang YM, He L, Zhou C and Liu RP (2018) Zircon U-Pb geochronology, geochemistry and geological significance of granites from the Sanfengshan Cu-Au deposit in Southern Beishan Orogenic Belt, Xinjiang. *Bulletin of Mineralogy, Petrology and Geochemistry* **37**, 294–306 (in Chinese with English abstract).
- Xu JW, Cao Y, Du YS, Wang GW and Pang ZS (2021) Generation and redox state of two episodes of Early Cretaceous granitoid in the Xiaoqinling area, North China Craton: implications for lithosphere thinning and metallogenic potential. *Lithos* **406–407**, e106538. doi: [10.1016/j.lithos.2021.106538](https://doi.org/10.1016/j.lithos.2021.106538).
- Yang CX and Santosh M (2020) Ancient deep roots for Mesozoic world-class gold deposits in the north China craton: an integrated genetic perspective. *Geoscience Frontiers* **11**, 203–14.
- Yang DB, Xu WL, Zhao GC, Huo TF, Shi JP and Yang HT (2016). Tectonic implications of Early Cretaceous low-Mg adakitic rocks generated by partial melting of thickened lower continental crust at the southern margin of the central North China Craton. *Gondwana Research* **38**, 220–37.
- Yang ZM, Chang ZS, Hou ZQ and Meffre S (2016) Age, igneous petrogenesis, and tectonic setting of the Bilihe gold deposit, China, and implications for regional metallogeny. *Gondwana Research* **34**, 296–314.
- Ye H, Zhang SH, Zhao Y and Wu F (2014) Petrogenesis and emplacement deformation of the Late Triassic Dushan composite batholith in the Yanshan fold and thrust belt: implications for the tectonic settings of the northern margin of the North China Craton during the Early Mesozoic. *Earth Science Frontiers* **21**, 275–92 (in Chinese with English abstract).
- Zhai MG and Santosh M (2011) The early Precambrian odyssey of the North China Craton: a synoptic overview. *Gondwana Research* **20**, 6–25.
- Zhang C, Ma CQ, Holtz F, Koepke J, Wolff PE & Berndt J (2013) Mineralogical and geochemical constraints on contribution of magma mixing and fractional crystallization to high-Mg adakite-like diorites in eastern Dabie orogen, East China. *Lithos* **172–173**, 118–38.
- Zhang C, Ma CQ, Liao QA, Zhang JY and She ZB (2011) Implications of subduction and subduction zone migration of the Paleo-Pacific Plate beneath eastern North China, based on distribution, geochronology, and geochemistry of Late Mesozoic volcanic rocks. *International Journal of Earth Science* **100**, 1665–84.
- Zhang SH, Zhao Y, Davis GA, Ye H and Wu F (2014) Temporal and spatial variations of Mesozoic magmatism and deformation in the North China Craton: implications for lithospheric thinning and decratonization. *Earth Science Reviews* **131**, 49–87.
- Zhang SH, Zhao Y, Liu JM, Hu JM, Song B, Liu J and Wu H (2010) Geochronology, geochemistry and tectonic setting of the Late Paleozoic-early Mesozoic magmatism in the northern margin of the North China block: a preliminary review. *Acta Petrologica et Mineralogica* **29**, 824–42 (in Chinese with English abstract).
- Zhang T, Zhang DH, Danyushevsky LV, Wu MQ, Alexis NK, Liao YZ and Zhang JL (2020) Timing of multiple magma events and duration of the hydrothermal system at the Yu'erya gold deposit, eastern Hebei Province,

- China: constraints from U–Pb and Ar–Ar dating. *Ore Geology Reviews* **127**, e103804. doi: [10.1016/j.oregeorev.2020.103804](https://doi.org/10.1016/j.oregeorev.2020.103804).
- Zhao G and Zhai M** (2013) Lithotectonic elements of Precambrian basement in the North China Craton: review and tectonic implications. *Gondwana Research* **23**, 1207–40.
- Zhou T, Goldfarb RJ and Phillips NG** (2002) Tectonics and distribution of gold deposits in China – an overview. *Mineralium Deposita* **37**, 249–82.
- Zorin YA, Zorina LD, Spiridonov AM and Rutshtein IG** (2001) Geodynamic setting of gold deposits in Eastern and Central Trans-Baikal (Chita Region, Russia). *Ore Geology Reviews* **17**, 215–32. doi: [10.1016/S0169-1368\(00\)00015-9](https://doi.org/10.1016/S0169-1368(00)00015-9).